

Lattice Discrete Particle Model (LDPM) for Failure Behavior of Concrete.

II: Calibration and Validation.

By

Gianluca Cusatis ¹, Andrea Mencarelli ², Daniele Pelessone ³, James Baylot ⁴

A Paper Submitted to
Cement & Concrete Composites
December 13, 2010
Corresponding Author
Gianluca Cusatis
Assistant Professor
Department of Civil and Environmental Engineering
4048 Johnsson Engineering Center
Rensselaer Polytechnic Institute
110 Eighth St
Troy, NY 12180-3590
Tel: (518) 276-3956
Fax: (518) 276-4833
e-mail: cusatg@rpi.edu

¹Corresponding Author: Assistant Professor, Department of Civil and Environmental Engineering, Rensselaer Polytechnic Institute, Troy (NY) 12180, USA. E-mail cusatg@rpi.edu, Phone: (518)-276-3956

²Graduate Student, Department of Civil and Environmental Engineering, Rensselaer Polytechnic Institute, Troy (NY) 12180, USA. E-mail: mencaa@rpi.edu

³Chief Scientist, Engineering and Software System Solutions, Inc. (ES3), San Diego (CA) 92101. E-mail: peless@es3inc.com

⁴Research Structural Engineer, U.S. Army Engineer Research and Development Center (ERDC), Vicksburg (MS) 39180. E-mail: James.T.Baylot@usace.army.mil

Report Documentation Page			Form Approved OMB No. 0704-0188	
<p>Public reporting burden for the collection of information is estimated to average 1 hour per response, including the time for reviewing instructions, searching existing data sources, gathering and maintaining the data needed, and completing and reviewing the collection of information. Send comments regarding this burden estimate or any other aspect of this collection of information, including suggestions for reducing this burden, to Washington Headquarters Services, Directorate for Information Operations and Reports, 1215 Jefferson Davis Highway, Suite 1204, Arlington VA 22202-4302. Respondents should be aware that notwithstanding any other provision of law, no person shall be subject to a penalty for failing to comply with a collection of information if it does not display a currently valid OMB control number.</p>				
1. REPORT DATE 13 DEC 2010	2. REPORT TYPE	3. DATES COVERED 00-00-2010 to 00-00-2010		
4. TITLE AND SUBTITLE Lattice Discrete Particle Model (LDPM) For Failure Behavior Of Concrete.II: Calibration And Validation			5a. CONTRACT NUMBER	
			5b. GRANT NUMBER	
			5c. PROGRAM ELEMENT NUMBER	
6. AUTHOR(S)			5d. PROJECT NUMBER	
			5e. TASK NUMBER	
			5f. WORK UNIT NUMBER	
7. PERFORMING ORGANIZATION NAME(S) AND ADDRESS(ES) U.S. Army Engineer Research and Development Center (ERDC),4Research Structural Engineer,Vicksburg,MS,39180			8. PERFORMING ORGANIZATION REPORT NUMBER	
9. SPONSORING/MONITORING AGENCY NAME(S) AND ADDRESS(ES)			10. SPONSOR/MONITOR'S ACRONYM(S)	
			11. SPONSOR/MONITOR'S REPORT NUMBER(S)	
12. DISTRIBUTION/AVAILABILITY STATEMENT Approved for public release; distribution unlimited				
13. SUPPLEMENTARY NOTES				
14. ABSTRACT The Lattice Discrete Particle Model (LDPM) formulated in the preceding Part I of this study is calibrated and validated in the present Part II. Calibration and validation is performed by comparing the results of numerical simulations with experimental data gathered from the literature. Simulated experiments include uniaxial and multiaxial compression, tensile fracture, shear strength, and cycling compression tests.				
15. SUBJECT TERMS				
16. SECURITY CLASSIFICATION OF:			17. LIMITATION OF ABSTRACT	
a. REPORT unclassified	b. ABSTRACT unclassified	c. THIS PAGE unclassified	Same as Report (SAR)	18. NUMBER OF PAGES 41
			19a. NAME OF RESPONSIBLE PERSON	

Abstract: The Lattice Discrete Particle Model (LDPM) formulated in the preceding Part I of this study is calibrated and validated in the present Part II. Calibration and validation is performed by comparing the results of numerical simulations with experimental data gathered from the literature. Simulated experiments include uniaxial and multiaxial compression, tensile fracture, shear strength, and cycling compression tests.

1 Introduction

The Lattice Discrete Particle Model (LDPM), formulated in Part I of this study [8], simulates concrete at the meso-scale by modeling the mechanical interaction of adjacent coarse aggregate pieces. The calibration of constitutive equations governing such interaction and the validation of the overall LDPM framework is pursued in the present Part II. Calibration and validation is performed by comparing the results of numerical simulations with experimental data gathered from the literature and relevant to uniaxial and multiaxial loading conditions in both tension and compression. The analysis of experimental data is restricted to the quasi-static regime in which time-dependent phenomena, such as creep and strain-rate effects, can be neglected. All the definitions and notations from Part I are retained herein.

2 Calibration and Validation

In this section, the procedure used to calibrate and validate the Lattice Discrete Particle Model (LDPM) is discussed. As presented in Part I of this study [8], LDPM response depends on two sets of parameters. The first set is relevant to the geometrical definition of concrete meso-structure and includes cement content, c , water-to-cement ratio, w/c , aggregate-to-cement ratio, a/c , maximum aggregate size, d_a , Fuller coefficient, n_F , and minimum aggregate size, d_0 . The first four parameters are obtained directly from the concrete mix design. The Fuller coefficient is identified by performing the best fitting (least square minimization was used in this study) of the experimental particle-size distribution, sieve curve. The last parameter (minimum aggregate size, d_0) governs the resolution of the model, which governs the number and direction of the possible crack paths in the meso-structure. Clearly, with a small minimum aggregate size, d_0 , it is possible to reproduce fine features of crack initiation and propagation in the mesostructure, but at the same time, the computational cost tends to be very high. In this study, a parametric analysis was performed to investigate the effect of the minimum aggregate size on the model's response for two typical test set-

ups: direct tension tests of dogbone-shaped specimens and uniaxial unconfined compression of cylindrical specimens. The mix design used consisted of cement content, c of 300 kg^3 , water-to-cement ratio, w/c of 0.5, aggregate-to-cement ratio, a/c of 6.5, Fuller coefficient, n_F of 0.5, and maximum aggregate size, d_a of 8. With a maximum aggregate size of 8 mm, the decrease of the minimum aggregate size from 4 mm to 1 mm, led to an increase in the percentage of simulated aggregate mass from about 30% to about 65% and to an increase of the number of computational particles from 1000 to 29000 for the cylinder and from 2300 to 61500 for the dogbone specimens (LDPM computational cost on a single processor is approximately proportional to the number of particles). The average peaks of the compression and tension tests varied about 17% and 4%, respectively. Somewhat higher variation was observed in the post-peaks, but the difference remained limited and was of about the same order of magnitude of the scatter of typical experimental data. However, one may also argue that LDPM parameters should actually change depending upon the selected minimum aggregate size. That is because the facet constitutive equations represent the behavior of finer scale phenomena associated with a particle size that is smaller than the minimum. This issue of selecting the minimum aggregate size in LDPM simulations is still open and is the subject of current research by the authors.

In the numerical calculations presented in this paper, the minimum aggregate size was selected to be as small as possible while keeping the computational cost reasonable. In any case, at least 30% of the total aggregate mass was simulated.

The second set of LDPM parameters that needs to be calibrated is relevant to the meso-scale parameters governing the facet constitutive law, as described in [8]. These parameters are described below along with their effect on the macroscopic model response.

- Normal elastic modulus (stiffness for the normal facet behavior), E_0 , and shear-normal coupling parameter (ratio between shear and normal elastic stiffness), α , govern LDPM response in the elastic regime. In particular, the macroscopic Poisson's ratio depends exclusively on α ; the typical concrete Poisson's ratio of about 0.18 can be obtained by setting $\alpha = 0.25$. Approximated analytical relationships between E_0 , α , and concrete macroscopic elastic parameters (Young's modulus E and Poisson's ratio ν) are reported in the companion paper [8].
- Tensile strength, σ_t , and the characteristic length, ℓ_t (or equivalently the tensile fracture energy, G_t ,

where $\ell_t = 2E_0G_t/\sigma_t^2$), govern the softening tensile fracturing behavior of LDPM facets and, consequently, govern all macroscopic behaviors featuring softening (e.g., tensile fracturing and unconfined and low-confined compression).

- Softening exponent, n_t , governs the interaction between shear and tensile behavior during softening at the facet level. More specifically it governs the rate at which facet tension-shear behavior transitions from softening (in pure tension) to plastic (in pure shear). At the macroscopic level, the softening exponent governs the difference in toughness or post-peak ductility observed during tensile and compressive failure simulations. By increasing n_t , one obtains more ductile behavior in both compression and tension, but the increase is (as a percentage) more pronounced in compression than in tension.
- Shear strength, σ_s , is the facet strength for pure shear and affects mostly the macroscopic behavior in compression (both unconfined and confined). In particular, the shear strength influences strongly the macroscopic unconfined compression strength but has no significant effect on the macroscopic tensile strength. Consequently, shear-to-tensile strength ratio, σ_s/σ_t , governs the ratio between the macroscopic compressive and tensile strengths.
- Yielding compressive stress, σ_{c0} , initial hardening modulus, H_{c0} , transitional strain ratio, κ_{c0} , and densified normal modulus, E_d , define the behavior of the facet normal component under compression and affect the macroscopic behavior in compression. In the case of a hydrostatic compression test, σ_{c0} governs the macroscopic volumetric stress at which yielding (pore collapse) begins; H_{c0} governs the slope of the volumetric stress-strain curve at the onset of yielding; and κ_{c0} governs the volumetric strain at which concrete starts to reharden due to material densification. Finally, E_d governs the tangent volumetric stiffness at very high levels of confinement as well as the volumetric unloading stiffness.
- Shear boundary parameters, i.e., initial internal friction coefficient, μ_0 , internal asymptotic friction coefficient, μ_∞ , and transitional stress, σ_{N0} , contribute to LDPM response in compression while they have basically no effect on tensile behavior. Internal asymptotic friction coefficient influences mainly the triaxial compressive behavior at high-confinement, and since the majority of experimental data

shows plateauing stress for increasing strain with high-confinement, $\mu_\infty = 0$ can be assumed in most cases.

- LDPM parameter κ_{c1} and κ_{c2} govern the nonlinear evolution of the normal facet stress in compression. Specifically, κ_{c1} is the deviatoric-to-volumetric strain ratio at which rehardening after pore collapse is prevented by deviatoric strain induced damage, and κ_{c1} determines the extent of this deviatoric effect on rehardening behavior.
- Densified modulus, E_d , is the facet unloading stiffness in compression during rehardening and, at the macroscopic level, governs unloading/reloading behavior for high-confinement compression.
- Finally, unloading-reloading parameter k_t determines the size of hysteresis cycles during unloading-reloading for the tensile fracturing facet behavior and governs the cyclic behavior at the macroscopic level in the case of both compressive and tensile behavior.

Calibration of LDPM parameters can be obtained through the best fitting of the complete load-displacement curves relevant to five different experimental tests: (1) hydrostatic compression; (2) unconfined compression; (3) fracture test; (4) triaxial compression at low-confinement; and (5) triaxial compression at high-confinement. In this work, the best fitting was performed through a heuristic “trial and error” procedure based on a visual assessment of the agreement between the experimental data (typically consisting of the averaged response of multiple samples) and the numerical result obtained by averaging the numerical response of three samples with distinct mesostructural geometries. Although automatic, more accurate, and more rigorous identification procedures available in the literature [18, 12] can be used (and they will be developed in future for LDPM), the adopted procedure led in most cases to a relatively accurate fit.

It must be noted that for the various experimental data sets analyzed in this study, the aforementioned experimental curves needed for the calibration were not always available. In these cases, the relevant LDPM parameters were either based on an “educated guess” or, when possible, estimated on the basis of experimental data available in the literature and relevant to concrete mixes similar to the one being simulated.

Specifically, fracture tests were not performed in most of the simulated experimental investigations. In

these cases, the calibration was obtained from estimates of the split (Brazilian) tensile strength, f'_t , based on the work of Arioglu et al. [1], and of the total fracture energy, G_F , based on the work of Bažant et al. [2]. In the numerical simulations, split tests and fracture tests were conducted by using the test setups shown in Figures 1a and 1b, respectively. Typical failure modes obtained in such simulations are shown in Figures 1c and 1d in which LDPM facets are colored according to values of the meso-scale crack opening defined as $w = (w_N^2 + w_M^2 + w_L^2)^{1/2}$, $w_i = \ell(\varepsilon_i - \sigma_i/E_i)$, and $i = N, M, L$. Consistently with known experimental evidence [21, 22], splitting tests are characterized by a splitting crack running along the specimen length, and dogbone fracture tests are characterized by a crack orthogonal to the applied load and located at the minimum cross section of the specimen. Typical load-displacement curves for splitting tests and fracture tests are shown in Figures 1e and 1f. The peak load of the split test was used to numerically compute the split tensile strength as $f'_{t,\text{NUM}} \approx 2P_u/(\pi BD)$, where D and B are diameter and length, respectively, of the split specimen (see Figure 1a). The area, W_F , under the load-displacement curve relevant to the fracture test was used to numerically compute the total fracture energy as $G_{F,\text{NUM}} \approx W_F/A_F$, where $A_F = dh$ is the minimum cross-sectional area of the fracture test specimen (Figure 1b). It must be recognized that this approach provides only an approximate estimate of the actual fracture properties because the split tensile strength and (more importantly) the total fracture energy are known to depend significantly on specimen shape, specimen size, and boundary conditions [24, 23, 36].

In addition, for several of the analyzed data sets, triaxial compression data under high-confinement were not available. In this case, LDPM parameters governing such behavior were assumed based on previous calibration experience of the authors. As a check, hydrostatic compression simulations were always performed with the assumed parameters, and it was checked that the numerical response was within the range of typical hydrostatic experimental data reported in the literature [11, 20, 32, 33, 14, 7, 17, 34, 35] shown in Figure 1g, where f'_c is compressive strength, Σ_V is macroscopic volumetric stress, E_V is macroscopic volumetric strain, $K_V = E/(1 - 2\nu)$ is volumetric modulus, E is Young's modulus, and ν is Poisson's ratio.

Finally, the validation of the model was performed (for each data set) by simulating experimental test results that were not used in the calibration phase but relevant to the same concrete. In the validation phase, parameter adjustments were not permitted.

3 Unconfined Compression

Experiments conducted by Van Mier and coworkers [29, 30] are simulated in this section in order to assess LDPM capability to simulate the behavior of concrete under unconfined compression. The experimental data are relevant to compression tests on prismatic specimens with the same cross-sectional area ($A=100 \times 100 \text{ mm}^2$) and different lengths (25 mm, 50 mm, 100 mm, and 200 mm). Basic material properties of the tested concrete mix are reported in the first column of Table 1. The load was applied through steel platens that were either directly in contact with the specimens ends (high friction condition) or had the contact surface covered with teflon sheets to reduce friction (low friction condition). In a related publication [31], the friction coefficient for teflon-to-concrete contact was measured as a function of the contact slippage (circles in Figure 2a); such dependence can be simulated through the equation $\mu(s) = \mu_d + (\mu_s - \mu_d)s_0/(s_0 + s)$ with $\mu_s = 0.03$, $\mu_d = 0.0084$, and $s_0 = 0.0195 \text{ mm}$ (solid curve in Figure 2a). This friction coefficient can be readily used to simulate frictional boundary conditions according to the simple algorithm discussed in a previous work by Cusatis et al. [9]. By using low friction parameters for the boundary conditions, LDPM parameters are calibrated by fitting the macroscopic response of low friction tests on the 100-mm-long specimens (and estimating fracture and triaxial parameters as per the discussion in the previous section). One can find the optimized parameters in the first column of Table 2. Finally, the calibration phase is completed by optimizing the high friction boundary condition parameters ($\mu_s = 0.13$, $\mu_d = 0.015$, and $s_0 = 1.3 \text{ mm}$) for untreated loading platens through the best fitting of the high friction tests on the 100-mm-long specimens. Figure 2b shows the obtained best fits for the low friction condition (curves labeled LF) and the high friction condition (curves labeled HF). The gray areas are the experimental results, and the black solid curves are relevant to the numerical simulations. In this section and in the rest of the paper, each numerical curve is the average of three numerical simulations obtained on specimens with different meso-structure (e.g., different random particle configuration). The load, P , was applied in the x_3 -direction, and the curves reported in Figure 2b (and all other figures relevant to the current section) visualize experimental data and numerical results in terms of macroscopic stress, $\Sigma_{33} = P/A$, and macroscopic strain, $E_{33} = \Delta L/L$, where ΔL is the specimen length change. Macroscopic stress components are symbolized in this section and throughout the paper with capitalized Greek letter instead of the more common lowercase Greek letters because the latter were used in Part I of this study

[8] to symbolize meso-scale variables. In addition, the first column of Table 3 reports the comparison between experimental macroscopic mechanical properties and the same numerically calculated properties. In Figure 2b as well as in Table 3, the agreement between experimental data and numerical results is excellent, but this is insufficient to assess the modeling capability of the model because such an agreement was obtained through parameter optimization. As it was mentioned earlier in this paper, only the simulation of experiments that were not used in the calibration phase can “validate” the model.

For this current set of data, the validation was performed by analyzing the lateral expansion of the 100-mm-long specimen and by simulating the responses of the 25-, 50-, and 200-mm-long specimens.

Figure 2c shows the macroscopic lateral strains E_{11} and E_{22} as functions of the macroscopic longitudinal strain E_{33} . The lateral strains were computed on the basis of the lateral displacements of one point on each lateral face of the specimens. This is consistent with the use of LVDTs (Linear Variable Differential Transformers) attached to opposite lateral faces of the specimens as were used in the experiments. The numerical results (solid curves) are in excellent agreement with the experimental results (gray areas) for low friction conditions. Although the numerical results for high friction conditions are on the higher side of the experimental data range, the agreement can be still considered very good. For $E_{33} \approx -0.2\%$, corresponding to the peak of the low friction case and while the high friction case is still in the pre-peak, the lateral strains are about 0.13% and 0.08% for low friction and high friction, respectively. These correspond to equivalent Poisson’s ratios in the inelastic regime equal to -0.65 and -0.4, respectively.

Figures 2d, 2e, and 2f show the comparison between experimental and numerical macroscopic stress-strain curves for the 25-, 50-, and 200-mm-long specimens. LDPM predicts remarkably well peak and post-peak responses for all three specimen sizes and for both low friction and high friction boundary conditions. Specifically, LDPM predicts correctly the increase of concrete strength due to the confinement caused by the frictional stresses at the specimen ends; such an increase is about 120% for the 25-mm-long specimen, 66% for the 50-mm-long specimen, and 7% for the 200-mm-long specimen.

Further evidence of the excellent modeling capability of LDPM is provided in Figure 3 where contours of meso-scale crack opening at failure are shown for low friction boundary condition (Figure 3a) and high friction boundary condition (Figure 3b). For the 200-mm-long specimens, low friction simulations predict failures characterized by localized cracks almost parallel to the applied load and trending from one end to

the other of the specimen. For the same specimens, high friction simulations are characterized by inclined cracks that leave the specimen ends mostly undamaged and have much less opening than the low friction case. Both results are consistent with published experimental data [30]. A similar trends are observed for the simulation of the shorter specimens even though, as the specimens become shorter, damage is more distributed, and a visual difference in the crack patterns is less appreciable.

To the authors' knowledge, no other model can predict stress-strain curves and failure modes under unconfined compression as well as LDPM. The main reason of such unique LDPM capability is that, unlike typical continuum-based concrete models, LDPM does not postulate the existence of softening in compression but rather simulates compressive failure through tensile and shearing softening at the meso-scale.

4 Biaxial Behavior

Experimental data relevant to the behavior of concrete under biaxial loading is considered here. The simulated experiments, published by Kupfer et al. [19], were conducted on 200-mm by 200-mm-square panels with out-of-plane thickness equal to 50 mm. Panels were made of plain concrete characterized by the mix design reported in the second column of Table 1. The biaxial loading condition was applied by means of steel brushes and in such a way that the ratio $k = \Sigma_{33}/\Sigma_{22}$ between the macroscopic stresses in two in-plane orthogonal directions was kept constant during each experiment.

Numerically, brush-type boundary conditions were simulated simply by frictionless boundary conditions. Experimental evidence [31] suggests that such an approach is accurate only up to the peak and that, in the post-peak, steel brushes do provide some degree of confinement. For this reason and because post-peak experimental data were not available from the experiments, the numerical simulations were not carried out far in the softening regime.

LDPM material parameters, reported in the second column of Table 2, were calibrated by the best fitting of the stress-strain curve for uniaxial compression ($k=-1/0$, right side of Figure 4a), the stress-strain curve for equi-biaxial compression ($k=-1/-1$, right side of Figure 4c), and by matching the estimated fracturing properties (f'_t and G_F) reported in the second column of Table 2. All the other experimental/numerical comparisons shown in Figure 4 can be considered validation of the model because they were

obtained without adjustments of model parameters.

In the left part of Figure 4a, one can see a comparison between the numerical and experimental lateral expansion (average of strains E_{11} and E_{22}) under uniaxial compression ($k=-1/0$). Figures 4b and 4c show the numerical results in direct tension ($k=1/0$) and equi-biaxial compression ($k=-1/-1$), respectively. Figures 4d and 4e report stress-strain curves relevant to compressive and tensile tests, respectively, in which the transverse stress Σ_{22} is about 50% (precisely 52% for compression and 55% for tension) of the vertical stress Σ_{33} . In Figure 4f, one can see the normalized (with respect to the compressive strength) experimental and numerical biaxial failure envelope. By looking at the presented results and by appreciating the excellent agreement between the experimental data and the numerical results for all of the different loading paths that were analyzed, one can conclude that LDPM, once calibrated, can predict very accurately concrete responses under biaxial loading conditions.

LDPM's modeling capability under biaxial loading, although impressive, is not unique because in the literature, there are other models [13, 10] that can perform as well as LDPM under these loading conditions. However, what is unique about LDPM is its capability, unlike other models, of correctly simulating the biaxial failure modes. This is demonstrated in Figure 4g in which contours of meso-scale crack opening for uniaxial tension ($k=1/0$), equi-biaxial tension ($k=1/1$), uniaxial compression ($k=-1/-1$, and compression with transverse tension ($k=-1/0.069$) are shown. These specific cases are selected here for discussion because in the experimental work [19], the relevant failure modes were reported. For uniaxial tension, failure is characterized by a single fracture orthogonal to the applied stress. For equi-biaxial tension, initially there are vertical and horizontal cracks that propagate from near the bottom left and top right corners of the specimen. These cracks eventually coalesce into an inclined crack running along one diagonal of the specimen. For uniaxial compression, failure is characterized by shear bands with an inclination of about 45°. Finally, in the case of compression/tension, the failure mode transitions from shear band to longitudinal splitting. All predicted failure modes are in agreement with the experimental observations.

In conclusion, it must be observed that LDPM's capability of predicting correctly the various failure modes is inherently associated with the fact that LDPM accounts for material heterogeneity. Clearly, classical continuum-based models cannot in any way capture damage localization and fracture in cases like the ones discussed above because, for these cases, classical continuum mechanics predicts uniform stress

and strain fields.

5 Triaxial Compression

Under triaxial compressive stresses, concrete materials show increased strength and ductility compared to the uniaxial case. This is mostly due to the effect of confinement, which makes concrete behavior transition from strain-softening, for unconfined and low-confinement situations, to strain-hardening, for high-confinement situations. Typical triaxial tests were carried out in U.S. Army Engineers Waterways Experiment Station (WES) and reported by Bažant and coworkers [5, 25]. They are performed on cylindrical specimens loaded through non-proportional loading paths. Specimens are first subjected to a hydrostatic pressure up to a target confining pressure p and then, while the pressure remains constant on the cylindrical surface, specimens are loaded longitudinally in either displacement or load control. These types of tests are analyzed in Section 5.1 for high-confinement and in Section 5.2 for low- and mild-confinement. In Section 5.3, less common proportional triaxial loading paths are analyzed. In this case, cubic specimens are subjected to stress states in which three orthogonal normal stresses have the same ratio during the loading process.

5.1 Non-Proportional Triaxial Loading Paths at High-Confinement

Numerical simulations of high-confinement triaxial experiments [5] are presented in this section. The tested cylindrical specimens were characterized by a length of 101.6 mm (4 in.) and a diameter of 50.8 mm (2 in.) and were cast with the mix design reported in the third column of Table 1. LDPM material parameters were calibrated on the basis of the experimental data relevant to hydrostatic compression, uniaxial unconfined compression, triaxial tests for $p = 20$ MPa and 200 MPa, and estimated fracturing properties (third column of Table 3). Experimental data relevant to other loading conditions were simulated for validation purposes. The optimized parameters are reported in the third column of Table 2. In the numerical simulations, the loading was applied longitudinally through the displacement of rigid loading platens in contact with the specimen ends (high friction contact conditions were assumed similar to those in the simulations in Section 3) whereas a pressure history was applied on the cylindrical surface of the specimens. The displacement history of the loading platens in the hydrostatic phase of the test was defined as to generate a pressure at

the top and bottom of the specimens equal to the pressure applied on the cylindrical surface.

Figure 5a shows a comparison between experimental data and numerical results for the hydrostatic test. Macroscopic volumetric stress, $\Sigma_V = (\Sigma_{11} + \Sigma_{22} + \Sigma_{33})/3$, is plotted against the macroscopic volumetric strain, $E_V = (E_{11} + E_{22} + E_{33})/3$ and, as one can see, the LDPM curve accurately fits the experimental data for both loading and unloading. Fitting of uniaxial compression experimental data is presented in Figure 5b. Triaxial simulations at various confinement levels (from 0 to 400 MPa) are reported in Figure 5c. The agreement between experimental data and numerical results is excellent not only for experimental data used in the calibration (confining pressure of 0, 20, and 200 MPa) but also for the data relevant to confining pressures equal to 100 and 400 MPa. Figure 5g shows the predicted failure modes for the triaxial tests. As previously shown in this paper, failure modes are visualized through coloring the LDPM facets according to the value of (positive) meso-scale crack openings. Figure 5g suggests that, for all different confining pressures, failure is ultimately associated with the development of tensile stresses in the mesostructure leading to cracking. For low-confinement, failure is characterized by the formation of shear inclined cracks; for high-confinement, failure is characterized by distributed cracks mainly oriented orthogonal to the longitudinal direction. It must be noted that such a result is in good agreement with very recent experimental data [20] and cannot be obtained through the adoption of macroscopic continuum-based models because such models predict, for the triaxial tests considered in this section, a purely compressive state of stress.

Figure 5d shows experimental data and numerical results relevant to a uniaxial strain test in which specimens are loaded in compression in the longitudinal direction while transverse expansion is prevented ($E_{11} = E_{22} = 0$). LDPM predicts accurately the response during both loading and unloading. Hydrostatic and uniaxial strain responses are compared (both for experiments and simulations) in Figure 5e in terms of macroscopic longitudinal stress-strain. In the elastic regime, the ratio between uniaxial strain stiffness and hydrostatic stiffness is $(1 - \nu)/(1 + \nu) \approx 0.7$ for $\nu = 0.18$. Such ratio decreases significantly during the inelastic evolution and, for example, it is about 0.5 for $E_{33} = 20 \times 10^{-3}$. LDPM, contrary to most models available in the literature, can capture accurately the stiffness decrease observed in the experiments. Finally, Figure 5f shows numerical simulation of a uniaxial strain test followed by transverse expansion at constant longitudinal strain, $E_{33} = \text{constant}$. Macroscopic longitudinal stress as well as macroscopic trans-

verse stresses are plotted against the macroscopic longitudinal strain for both experiments and numerical simulations. During the loading phase, the results of numerical simulations are in good agreement with the experimental data as far the transverse behavior is concerned but it seems to underestimate the longitudinal stress. However, it must be noted that during the loading phase, this test coincides with the uniaxial strain test reported in Figure 5d and clearly the results of two experiments are not consistent. For example, for $E_{33} = -30 \times 10^{-3}$, $\Sigma_{33} = -330$ MPa in one case, and $\Sigma_{33} = -380$ MPa in the other. During the transverse expansion phase, both the longitudinal and transverse stresses relax completely to zero.

5.2 Non-Proportional Triaxial Loading Paths at Low-Confinement

This section discusses concrete response under non-proportional triaxial loading paths at low-confinement. The simulated experiments [25] were conducted on concrete cylinders with length equal to 300 mm and diameter equal to 150 mm. Loading was applied similarly to what discussed in the previous section, but the contact between the loading platens and the specimens was characterized by low friction conditions (see Section 3) because friction-reducing teflon sheets were used in the experimental set-up. The concrete mix design relevant to the tested specimens is in the fourth column of Table 1. Adopted LDPM parameters and macroscopic mechanical properties are reported in the fourth column of Table 2 and Table 3, respectively. LDPM parameter calibration was obtained by simulating unconfined compression tests, triaxial tests with confining pressure $p = 4.5$ MPa and 60 MPa, and estimated hydrostatic and fracturing data.

Figure 6a shows the comparisons of experimental data and numerical results relevant to the uniaxial unconfined compression test. The macroscopic longitudinal stress, Σ_{33} , is plotted against the macroscopic longitudinal strain, E_{33} , and the macroscopic transverse strains, $E_{11} = E_{22}$. The transverse strains were calculated on the basis of the volume variation, ΔV , as $E_{11} = E_{22} = 0.5(\Delta V/V_0 - E_{33})$, where V_0 =initial specimen volume, as opposed to local displacements for reasons discussed later. Figure 6b reports the triaxial results for confining pressures from 0 to 60 MPa. The agreement is generally satisfactory even though for very low-confinement level, the numerical results tend to predict a more ductile behavior as shown by the stress-strain curves for confining pressures up to 9 MPa.

The issue of lateral expansion is illustrated in Figure 6c with reference to the response of only one specimen, as opposed to the average response of three specimens in the other figures, subjected to a confining

pressure of 4.5 MPa. In this figure, lateral strains, computed on the basis of the radial displacements of four points A, B, C, and D located on the surface of the specimen are plotted against the longitudinal strain. The four curves coincide for very small longitudinal strains (basically in the elastic regime) while they diverge in the inelastic phase. For example, for a longitudinal strain equal to -3×10^{-3} , the calculated lateral strains range from about 1 to 2×10^{-3} . The difference in the lateral strains calculated at different points is due to the heterogeneous response of concrete and, most importantly, to anisotropic damage localization occurring in the post-peak. For this reason, the lateral strains plotted in Figures 6a and 6d are computed in the average sense through the volume variation of the specimens. It must be noted that the relevant experimental results are actually relevant to the average of two strain gages measurements and that, due to the way the strain gages were attached to the specimen surface, the experimental data is actually neither local, as results in Figure 6c, nor global, as the calculated lateral strains based on the volume variation. Nevertheless, based on the experimental versus numerical comparison shown in Figure 6d, one can conclude that the numerical results agree well with the experimental evidence. Finally, 6e shows contours of meso-scale crack opening at failure for the unconfined case (left) and for a confinement of 4.5 MPa (right). Similar failure modes were observed in the experiments [25].

5.3 Proportional Triaxial Loading Paths

The analysis of concrete triaxial behavior is completed in this section by simulating triaxial tests by Van Mier [28]. In these experiments, cubic specimens (whose composition is in the fifth column of Table 1) were loaded in three orthogonal directions (x_1 , x_2 , and x_3) by keeping the stress ratios $k_1 = \Sigma_{11}/\Sigma_{33}$ and $k_2 = \Sigma_{22}/\Sigma_{33}$ constant during the loading process.

In the experiments, loading was applied by means of steel brushes. In Section 4, loading with brushes was simulated through frictionless boundary conditions because the interest was mainly for the behavior up to peak. In this section, such a simplification is not acceptable because the experimental data provide information about the post-peak behavior and, as mentioned earlier in this paper and well documented in the literature [31], brushes do provide a certain degree of confinement in the post-peak. This confinement can be approximately simulated through the same frictional contact algorithm used in Section 3 and assuming $\mu_s = 0$, $\mu_d = 0.035$, and $s_0 = 0.00005$ mm. These parameters were determined based on experimental data reported in the literature [28]. LDPM parameter calibration (fifth column of Table 2)

was performed by simulating uniaxial compression, triaxial compression with $k_1 = 0.1$ and $k_2 = 0.1$, and estimated hydrostatic and fracturing properties (fifth column of Table 3).

Figure 7a shows the comparison between experimental results and numerical simulations for the case of uniaxial compression. The comparison is relevant to cubic specimens (curve labeled $L = 100$ mm) as well as prismatic specimens with the same cross sectional area of the cube (100 mm by 100 mm) and two different lengths (curves labeled $L = 50$ mm and $L = 200$ mm). The numerical results agree very well with the experimental data and, similarly to the results in Section 3, they capture correctly the increased strength and ductility for decreasing specimen length.

In Figures 7b, 7c, and 7d one can see comparisons between experimental results and numerical simulations in terms of macroscopic stress Σ_{33} against macroscopic strains E_{33} , E_{22} , and E_{11} , respectively. Each plot reports macroscopic stress-strain curves for three different loading paths characterized by $k_1 = 0.1$ and $k_2 = 0, 0.1$, and 0.33 , respectively. Overall the agreement between experiments and numerical simulations is good. LDPM captures well the increase strength (peak stress) for increasing k_3 ratio. Less satisfactory agreement can be observed in the post-peak behavior in which LDPM's response is generally more ductile than the experimental evidence. Future research will clarify whether this is a shortcoming of the current LDPM formulation or the discrepancies caused by the simplified approach used to simulate the effect of the loading steel brushes.

Finally, Figure 7e shows meso-scale crack opening contours for uniaxial compression (on the left) and for $k_2 = 0.33$ (on the right). As one can see, failure in uniaxial compression is characterized mainly by splitting cracks, i.e., cracks parallel to the applied load, whereas in the triaxial case, one can see V-shaped cracks in the $x_1 - x_3$ plane. Similar crack patterns are reported in the original experimental publication [28].

6 Torsional-Compressive Behavior

The numerical simulations presented in this section are relevant to the behavior of concrete subject to combined macroscopic compressive and shearing stresses. The simulated experiments [6] were conducted on concrete cylinders of length equal to 762 mm (30 in.) and diameter equal to 228.6 mm (9 in.). The top and bottom parts of the specimens were clamped as shown in Figure 8d and thus the actual length of the

tested specimens was 444.5 mm (17.5 in.). The concrete mix design used in the experimental program is shown in the sixth column of Table 1. LDPM parameters were calibrated by fitting the reported uniaxial unconfined strength ($f_p = 29.5$ MPa measured on the same specimens tested under combined loads) and by fitting the reported modulus of rupture (measured on 152.4-mm by 152.4-mm by 508-mm prismatic specimens). Estimated fracturing and hydrostatic data were also used for parameter calibration. Mesoscale LDPM parameters and macroscopic mechanical properties are reported in the sixth column of Table 2 and Table 3, respectively. It must be noted that the unconfined strength f_p is not equal to the compressive strength f'_c measured on 304.8-mm by 152.4-mm (12 in. by 6 in.) specimens (typically used in standard compressive strength tests), due to the size effect. In the considered experimental program, f'_c was 32.89 MPa (See Table 3).

Specimens were loaded through non-proportional loading paths in which specimens were first loaded in compression up to a given level of stress, and then, at constant compression, specimens were subject to torsion. Figure 8a shows longitudinal macroscopic stress versus longitudinal macroscopic strain for uniaxial unconfined compression and for compression-torsion tests characterized by a compressive stress equal to 0.2, 0.4, 0.6, 0.8, and 0.9 times compressive strength f_p . It is interesting to note that, especially for compressive stresses higher than 50% of f_p , results show increasing longitudinal macroscopic strain at constant longitudinal macroscopic stress, which means that the increase strain is caused by the applied torsion.

Figure 8b shows nominal macroscopic torsional stress, Σ_T , versus nominal macroscopic torsional strain, E_T , curves for the various levels of compression. Torsional stress is defined as $\Sigma_T = 16T/(\pi d^3)$, where T is the applied torque and d is the diameter of the specimens. Torsional strain is defined as $E_T = \theta d/(2L)$, where θ =angle of twist and L =specimen length. Torsional strength, defined as peak torsional stress, increases as a function of the level of compression for compressive stresses up to 50% of f_p ; torsional strength decreases for compressive stresses higher than 50% of f_p . Figure 8b also shows a reduction of the shear stiffness for increasing applied macroscopic compressive stresses. This phenomenon, known as “vertex effect”, is well documented in the literature, and only a limited number of models are successful in simulating it [5].

Numerical results are compared with experimental data in Figure 8c in terms of normalized failure

domain that represents change of torsional strength as a function of applied compression. Agreement is overall satisfactory. Finally, one can see in Figure 8d meso-scale crack opening contours at failure for pure torsion, and for combined compression-torsion loading at two levels of compressive stresses (40% and 80% of f_p). For pure torsion, failure is characterized by a localized helicoidal tensile fracture. For a compressive stress equal to 40% of f_p , failure is still characterized by a helicoidal fracture that, however, is more distributed compared to pure torsion. Finally, for a compressive stress equal to 80% of f_p , failure mode is different and is characterized by crushing of the central part of the specimen. This is the failure mode observed in the experiments in pure compression. Similar trends and similar modes of failure were observed in the experiments.

7 Cyclic Behavior

Concrete behavior under cycling loading is considered herein in relation to the experimental program on cyclic uniaxial compression tests carried out by Sinha et al. [26, 27]. Tested specimens were cylinders with a radius of 76.2 mm (1.5 in.) and length of 152.4 mm (6 in.). The adopted mix design is summarized in the seventh column of Table 1. Model parameters were calibrated on the basis of the monotonic uniaxial compression test as well as estimated hydrostatic and fracturing properties. The parameter governing the cyclic behavior (k_t in Table 2) was calibrated by fitting one unloading-reloading cycle from the macroscopic stress-strain curve (Figure 9b). Optimized meso-scale parameters are in the seventh column of Table 2. Macroscopic experimental and numerical mechanical parameters are listed in the seventh column of Table 3. Figure 9a shows the macroscopic longitudinal stress-strain curve for both experiments and numerical simulations under monotonic loading. The macroscopic strain was measured with a measured length of 105.41 mm in the central part of the specimen. The response under cyclic compression is in Figure 9b in which four unloading-reloading cycles were performed. LDPM predicts, in agreement with the experimental data, hysteretic cycles whose width increases with increasing macroscopic strain. Finally, for comparison, a load-displacement curve for a dogbone specimen subject to cyclic tension is in Figure 9c. The response is realistic in terms of both shape and width of hysteretic cycles.

8 Tensile Fracturing Behavior

The experimental program relevant to three-point bending tests on concrete notched beams performed by Horvath and Persson [16] is analyzed in this section in order to evaluate the ability of LDPM to simulate tensile fracturing behavior. Reported experiments investigated the effect of specimen size on fracturing response of concrete, and three specimens sizes were considered as shown in Figure 10. These specimens, labeled as “small”, “medium”, and “large”, were characterized by depth, D , equal 100 mm, 200 mm, and 300 mm, respectively, span, S , equal 800 mm, 1131 mm, and 1386 mm, respectively, and thickness, B , equal to 100 mm. All the specimens were notched with half-depth 4-mm-wide notches. Since damage was expected in the vicinity of the notch tip, LDPM was used only in the 100-mm-wide central part of the specimens whereas the lateral parts were modeled through classical elastic finite elements (Figure 10). This led to a significant reduction of the computational cost of the simulations. LDPM and finite element regions were connected through a master-slave algorithm.

The mix design used in the experimental program is in the eighth column of Table 1. LDPM parameters were calibrated by fitting the load-displacement curve for the medium specimens and the compressive strength, f'_c , measured in 150-mm-side cubes (Table 3). In addition, estimated hydrostatic compression tests were used for the calibration. Table 2 and Table 3 report LDPM calibrated parameters and macroscopic material properties, respectively.

Comparisons between experimental and numerical load-displacement curves are shown in Figures 11a, 11b, and 11c for the different specimens sizes. Agreement between experiments and numerical simulations is excellent for all three specimen sizes as far as peak load is concerned. It is also excellent for the post-peak curves relevant to medium- and large-size specimens (Figures 11a and 11b). For the post-peak behavior of the small-size specimens (Figure 11c), the numerical results tend to overestimate material toughness. This is probably caused by the fact that the ligament of the small-size specimens is only 50 mm while the maximum and minimum aggregate size used in the simulations are 16 mm and 5 mm, respectively. As one can see, only a few aggregate pieces actually fit along the ligament. This led, most probably, to a lack of resolution of the crack pattern. Adoption of a smaller minimum aggregate size would have improved the result, but it would have increased the computational cost of the simulations tremendously for the medium- and large-size specimens. Similar discussion applies to Figure 11d in which experiments and numerical

results are shown for the response of dogbone specimens loaded in tension and characterized by a ligament area of 50 by 50 mm². Again, agreement is excellent for the peak load and somewhat less accurate, but still satisfactory, in the post-peak response. It must be noted that results in Figures 11b, 11c, and 11d are actual model predictions since those experiments were not used in the calibration phase. Finally, Figure 11e show contours of meso-scale crack opening in which one can see a crack band, as opposed to a single localized crack, developing from the notch tip and propagating towards the opposite specimen side. It is also worth noting that for the three different sizes, the width of the crack band does not change. This is in agreement with typical experimental evidence reported in the literature [4].

9 Tensile Splitting Strength Tests

The experimental program of splitting (Brazilian) tensile tests performed by Bažant et al. [3] is simulated here. These experiments investigated the effect of specimen size (size effect) on concrete tensile strength, f'_t . The different diameters used were 19 mm (0.75 in.), 38 mm (1.5 in.), 76 mm (3 in.), 152 mm (6 in.), 254 mm (10 in.), and 508 mm (20 in.). Specimen heights were 51 mm (2 in.) for all specimens. Figure 12 shows the LDPM models used for the various specimens. Basic material properties relevant to this experimental program are in the last column of Table 1. LDPM parameters were calibrated by fitting the tensile splitting response of the specimens with a diameter equal to 76 mm and the compressive strength (Table 3) measured on 76 mm (3 in.) by 152 mm (6 in.) cylindrical specimens. In addition, estimates of fracture energy and hydrostatic response were used for the calibration.

Figure 13a shows nominal stress, defined as $2P/(\pi BD)$, versus displacement curves obtained in the numerical simulations. The peaks of the nominal stress is the tensile splitting strength. Dependence of splitting strength as a function of specimen size is shown in Figure 13b where experimental data are also shown. Numerical results are in very good agreement with the experimental results for specimen sizes of 19 mm, 38 mm, and 508 mm. For specimen sizes of 152 mm and 254 mm, LDPM seems to overestimate the experimental strength. However, it must be observed that contrary to the numerical results, experimental data in this size range exhibits a violation of the size-effect trend. Such a violation was explained by the observation that the intermediate-size specimens were characterized by a different failure mechanism. While smaller and larger specimens failed due to a splitting crack initiating in the center of the specimens,

intermediate-size specimens seemed to develop significant damage underneath the loading platens. All numerically simulated specimens failed with crack developing from the central part of the specimens, as shown in Figure 13c, where meso-scale crack opening contours at failure are shown for one specimen of size D equal to 38 mm.

In splitting tests, different modes of failure can be associated with different ways of applying the load [15]. Unfortunately, the experimental publication does not specify details relevant to the application of load. The best guess of the authors is that specimens were loaded in direct contact with steel loading platens. This makes the loaded area increase somewhat with specimen size since larger specimen diameters are associated with smaller curvature of the external surface of the specimen. This effect was not simulated in the numerical simulations, and it might be the cause of the discrepancy observed in the response of the intermediate-size specimens. A more detailed analysis of these experimental data is the subject of future research by the authors.

10 Conclusions

The Lattice Discrete Particle Model (LDPM) was formulated in Part I of this study and was extensively calibrated and validated in the present Part II. LDPM simulates concrete at the length scale of coarse aggregate pieces (meso-scale) and is formulated within the framework of discrete models, which enable capturing the salient aspects of material heterogeneity while keeping the computational cost manageable.

Based on the results presented in this study, the following conclusions can be formulated.

1. LDPM simulates accurately the behavior of concrete under unconfined compression. It succeeds in the ambitious goal of simulating strain-softening in compression without postulating compressive softening behavior in the constitutive equations. LDPM softening response under unconfined compression is governed mainly by tensile fracturing and cohesive/frictional shearing at the meso-scale. It reproduces with great accuracy the effect on specimen length predicting stronger and more ductile behavior for shorter specimens. It models well the effect of frictional boundary conditions on compressive strength and post-peak ductility. In addition, LDPM predicts correctly the formation of splitting cracks for boundary conditions with low friction and shear-band type fracture for high friction boundary conditions. It predicts the correct lateral expansion in the post-peak phase.

2. LDPM provides accurate representations of concrete behavior under biaxial loading conditions. It simulates correctly concrete strength under biaxial compression and biaxial tension. It reproduces very well the biaxial failure envelope as well as macroscopic stress-strain relationships. It predicts typical biaxial modes of failure characterized by complex fracture paths.
3. LDPM can simulate concrete behavior under triaxial loading. It predicts increased strength and ductility with increasing confinement for both proportional and non-proportional loading paths. It reproduces yielding and stiffness recovery well under hydrostatic compression. It can model stiffness increase upon unloading from very high confining pressure.
4. LDPM is accurate in predicting the increase/decrease of torsional shear strength as a function of compression. It predicts an increase in shear strength for compressive stresses up to about 50% of the compressive strength and a decrease of shear strength for higher compressive stresses. In addition, LDPM reproduces the so-called “vertex effect” that is the reduction of shear stiffness as a function of the normal compressive stress. LDPM models correctly transition the mode of failure from pure shear conditions (characterized by an inclined tensile fracture) to pure compression (characterized by shear banding and concrete crashing).
5. LDPM provides accurate representation of concrete behavior under cycling loading both in tension and unconfined, confined, and hydrostatic compression. It is able to reproduce the slope of the unloading phase and the width of the hysteresis cycle.
6. LDPM can simulate tensile fracturing as demonstrated by the successful simulation of three-point bending tests on notched specimens. It is able to reproduce pre-peak nonlinearity as well as softening post-peak behavior. It reproduces realistically the development of a crack pattern due to tensile stresses. It predicts correctly size effect on specimen load carrying capacity.
7. LDPM can simulate macroscopic tensile strength of concrete as measured through tensile splitting (Brazilian) tests. It predicts size effect on concrete tensile strength and reproduces well splitting failure modes typically observed in the experiments.

Acknowledgment: This effort was sponsored by the US Army Engineer Research and Development

Center. Permission to publish was granted by the Director, Geotechnical and Structures Laboratory. The work of first author was also supported under NSF grant No 0928448 and DTRA grant No HDTRA1-09-1-0029 to Rensselaer Polytechnic Institute.

References

- [1] N. Arioglu, Z. C. Girgin, and E. Arioglu. Evaluation of ratio between splitting tensile strength and compressive strength for concretes up to 120 mpa and its application in strength criterion. *Aci Materials Journal*, 103(1):18–24, 2006.
- [2] Z. P. Bazant and E. Becq-Giraudon. Statistical prediction of fracture parameters of concrete and implications for choice of testing standard. *Cement and Concrete Research*, 32(4):529–556, 2002.
- [3] Z. P. Bazant, M. T. Kazemi, T. Hasegawa, and J. Mazars. Size effect in brazilian split-cylinder tests - measurements and fracture-analysis. *Aci Materials Journal*, 88(3):325–332, 1991.
- [4] Z. P. Bazant and B.-H. Oh. Crack band theory for fracture of concrete. *Materials and Structures (RILEM, Paris)*, 16:155177, 1983.
- [5] Z. P. Bazant, Y. Y. Xiang, M. D. Adley, P. C. Prat, and S. A. Akers. Microplane model for concrete .2. data delocalization and verification. *Journal of Engineering Mechanics-Asce*, 122(3):255–262, 1996.
- [6] B. Bresler and K. S. Pister. Strength of concrete under combined stresses. *Journal of the American Concrete Institute*, 30(3):321–345, 1958.
- [7] F. C. Caner and Z. P. Bazant. Microplane model m4 for concrete. ii: Algorithm and calibration. *Journal of Engineering Mechanics*, 126(9):954, 2000.
- [8] C. Cusatis, D. Pelessone, and A. Mencarelli. Lattice discrete particle model (ldpm) for failure concrete behavior. i: Theory. *Cement and Concrete Composites, submitted*, 2010.
- [9] G. Cusatis, Z. P. Bazant, and L. Cedolin. Confinement-shear lattice model for concrete damage in tension and compression: Ii. computation and validation. *Journal of Engineering Mechanics-ASCE*, 129(12):1449–1458, 2003.

- [10] P. Grassl, K. Lundgren, and K. Gylltoft. Concrete in compression: a plasticity theory with a novel hardening law. *International Journal of Solids and Structures*, 39(20):5205–5223, 2002.
- [11] S. J. Green and S. R. Swanson. Static constitutive relations for concrete. *Technical rept. Sep 1970-Nov 1972*, 1973.
- [12] M. Grewal and A. Andrews. *Kalman filtering: Theory and practice using MATLAB*. 3ed., Wiley-IEEE, 2008.
- [13] S. Gupta. Importance of multiple damage model for analysis of rc structures. *Fracture Mechanics of Concrete Structures, Vols 1 and 2*, pages 565–572 1089, 2001.
- [14] S. J. Hanchak, M. J. Forrestal, E. R. Young, and J. Q. Ehrgott. Perforation of concrete slabs with 48-mpa (7-ksi) and 140-mpa (20-ksi) unconfined compressive strengths. *International Journal of Impact Engineering*, 12(1):1–7, 1992.
- [15] T. Hasegawa, T. Shioya, and T. Okada. Size effect on splitting tensile strength of concrete, 1985.
- [16] R. Horvath and T. Persson. *The influence of the size of the specimen on the fracture energy of concrete*. PhD thesis, Lund Institute of Technology, 1984.
- [17] S Joy and R. Moxley. Material characterization, wsmr-5 3/4-inch concrete. Technical report, US Army Engineer Waterways Experiment Station, August 1993 1993.
- [18] R. E. Kalman. A new approach to linear filtering and prediction problems. *Transaction of the ASME-Journal of Basic Engineering*, pages 35–45, 1960.
- [19] H. Kupfer, H.K. Hilsdorf, and H. Rusch. Behaviour of concrete under biaxial stresses. *ACI Journal*, 66:656–666, 1969.
- [20] C. Poinard, Y. Malecot, and L. Daudeville. Damage of concrete in a very high stress state: experimental investigation. *Materials and Structures*, 43(1-2):15–29, 2010.
- [21] C. Rocco, G. V. Guinea, J. Planas, and M. Elices. Experimental analysis of rupture mechanisms in the brazilian test, 1998.

- [22] C. Rocco, G. V. Guinea, J. Planas, and M. Elices. Mechanisms of rupture in splitting tests. *Aci Materials Journal*, 96(1):52–60, 1999.
- [23] C. Rocco, G. V. Guinea, J. Planas, and M. Elices. Size effect and boundary conditions in the brazilian test: Experimental verification. *Materials and Structures*, 32(217):210–217, 1999.
- [24] C. Rocco, G. V. Guinea, J. Planas, and M. Elices. Size effect and boundary conditions in the brazilian test: Theoretical analysis. *Materials and Structures*, 32(220):437–444, 1999.
- [25] D. Sfer, I. Carol, R. Gettu, and G. Etse. Study of the behavior of concrete under triaxial compression. *Journal of Engineering Mechanics-Asce*, 128(2):156–163, 2002.
- [26] B. P. Sinha. *The inelastic behaviour of plain and reinforced concrete under cyclic loading*. PhD thesis, University of Colorado, 1962.
- [27] B. P. Sinha, K. H. Gerstle, and L. G. Tulin. Stress-strain relations for concrete under cyclic loading. *J. Amer. Concr. Inst.*, 61(2):195–210, 1964.
- [28] J. G. M. Van Mier. Multiaxial strain-softening of concrete part i: Fracture. *Materials and Structures*, 19(3):179–190, 1986.
- [29] J. G. M. Van Mier, S. P. Shah, M. Arnaud, J. P. Balyssac, A. Bascoul, S. Choi, D. Dasenbrock, G. Ferrara, C. French, M. E. Gobbi, B. L. Karihaloo, G. Konig, M. D. Katsovos, J. Labuz, D. Lange-Kornbak, G. Markeset, M. N. Pavlovic, G. Simsch, K. C. Thienel, A. Turatsinze, M. Ulmer, H. J. G. M. Van Geel, M. R. A. Van Vliet, and D. Zissopoulos. Strain-softening of concrete in uniaxial compression - report of the round robin test carried out by rilem tc 148-ssc. *Materials and Structures*, 30(198):195–209, 1997.
- [30] M. R. A. Van Vliet and J. G. M. Van Mier. Experimental investigation of concrete fracture under uniaxial compression. *Mechanics of cohesive-frictional materials*, 1:115–127, 1996.
- [31] R. A. Vonk. *Softening of Concrete Loaded in Compression*. PhD thesis, Eindhoven University of Technology, 1992.

- [32] X. H. Vu, Y. Malecot, L. Daudeville, and E. Buzaud. Effect of the water/cement ratio on concrete behavior under extreme loading. *International Journal for Numerical and Analytical Methods in Geomechanics*, 33(17):1867–1888, 2009.
- [33] X. H. Vu, Y. Malecot, L. Daudeville, and E. Buzaud. Experimental analysis of concrete behavior under high confinement: Effect of the saturation ratio. *International Journal of Solids and Structures*, 46(5):1105–1120, 2009.
- [34] J. H. Weathersby. Investigation of bond slip between concrete and steel reinforcement under dynamic loading conditions. Technical Report ERDC/GSL TR-03-9, US Army Corps of Engineers, 2003.
- [35] E. M. Williams, S. S. Graham, P. A. Reed, and T. S. Rushing. Laboratory characterization of cor-tuf concrete with and without steel fibers. Technical report, U.S. Army Engineer Research and Development Center, May 2009 2009.
- [36] F. H. Wittmann, H. Mihashi, and N. Nomura. Size effect on fracture energy of concrete. *Engineering Fracture Mechanics*, 35(1-3):107–115, 1990.

Symbol [Units]	Sec. 3	Sec. 4	Sec. 5.1	Sec. 5.2	Sec. 5.3	Sec. 6	Sec. 7	Sec. 8	Sec. 9
c [Kg/m ³]	375	190	264	349	320	311	279	612	686
w/c [-]	0.5	0.9	0.553	0.57	0.5	0.51	0.69	0.4	0.5
a/c [-]	4.8	10.7	7.1	5.3	6	6.4	6.74	2.42	2
ρ [Kg/m ³]	2370	2400	2290	2400	2400	2460	2352	2338	2400
d_a [mm]	8	15	9.5	20	16	12.7	9.5	16	5
n_F [-]	0.55	0.45	0.5	0.72	0.44	0.58	0.5	0.41	0.5

Table 1: Values of parameters governing the generation of concrete meso-structure.

Symbol [Units]	Sec. 3	Sec. 4	Sec. 5.1	Sec. 5.2	Sec. 5.3	Sec. 6	Sec. 7	Sec. 8	Sec. 9
d_0 [mm]	4	4	4	10	6	7	4	5	2
$1 - F(d_0)$ [-]	0.32	0.45	0.35	0.39	0.31	0.30	0.35	0.38	0.37
E_0 [MPa]	43748	46260	38636	43195	49455	46480	32081	60273	55610
α [-]	0.25	0.25	0.25	0.25	0.25	0.25	0.25	0.25	0.25
σ_t [MPa]	4.03	3.04	4.16	4.6	4.5	2.65	3.7	3.44	4.65
l_t [mm]	120	100	100	200	120	200	50	500	100
$(G_t \text{ [N/m]})^\dagger$	(22.3)	(10)	(22.4)	(49)	(24.6)	(15.1)	(10.7)	(49.1)	(19.4)
σ_s/σ_t [-]	2.7	5.75	2.7	2.35	2.75	4.1	1.9	2.60	2.75
n_t [-]	0.2	0.2	0.2	0.2	0.2	0.2	1	0.4	0.1
σ_{c0} [MPa]	150	35	120	100	120	100	100	150	150
H_{c0}/E_0 [-]	0.4	0.1	0.67	0.6	0.4	0.4	0.4	24109	22244
κ_{c0} [-]	2	4	3.8	4	2	4	4	4	4
κ_{c1} [-]	1	1	1.2	1	1	1	1	1	1
κ_{c2} [-]	5	5	5	5	5	5	5	5	5
μ_0 [-]	0.2	0.05	0.4	0.16	0.2	0.2	0.2	0.4	0.4
μ_∞ [-]	0	0	0	0.16	0	0	0	0	0
σ_{N0} [MPa]	600	600	600	600	600	600	600	600	600
k_t [-]	-	-	-	-	-	-	0.8	-	-
E_d/E_0 [-]	1	1	1.81	1	1	1	1	1	1

Table 2: Values of material model parameters used in the numerical simulations. $\dagger G_t = \ell_t \sigma_t^2 / (2E_0)$

Symbol [Units]	Sec. 3	Sec. 4	Sec. 5.1	Sec. 5.2	Sec. 5.3	Sec. 6	Sec. 7	Sec. 8	Sec. 9
f'_c [MPa]	38.35	32.06	45.70	35.80	42.05	33.22	25.86	68	51.4
f'_t [MPa]	3.85†	2.89†	4.30†	3.70†	4.19†	3.44† / 4.55§	3.00†	-	-
G_F [N/m]	51-95‡	42-78‡	55-101‡	76-141‡	58-107‡	50-92‡	39-73‡	-	80-104
$f'_{c,\text{NUM}}$ [MPa]	40.09	32.36	47.65	35.09	41.08	32.89	26.24	67.8	53.7
$f'_{t,\text{NUM}}$ [MPa]	3.86	2.81	4.28	3.70	4.32	3.41 / 4.69	3.04	-	-
$G_{F,\text{NUM}}$ [N/m]	92	53	97	133	98	63	80	-	97

Table 3: Values of macroscopic mechanical properties. † Estimated from [1]. ‡ Estimated from [2]. § Obtained from modulus of rupture test.

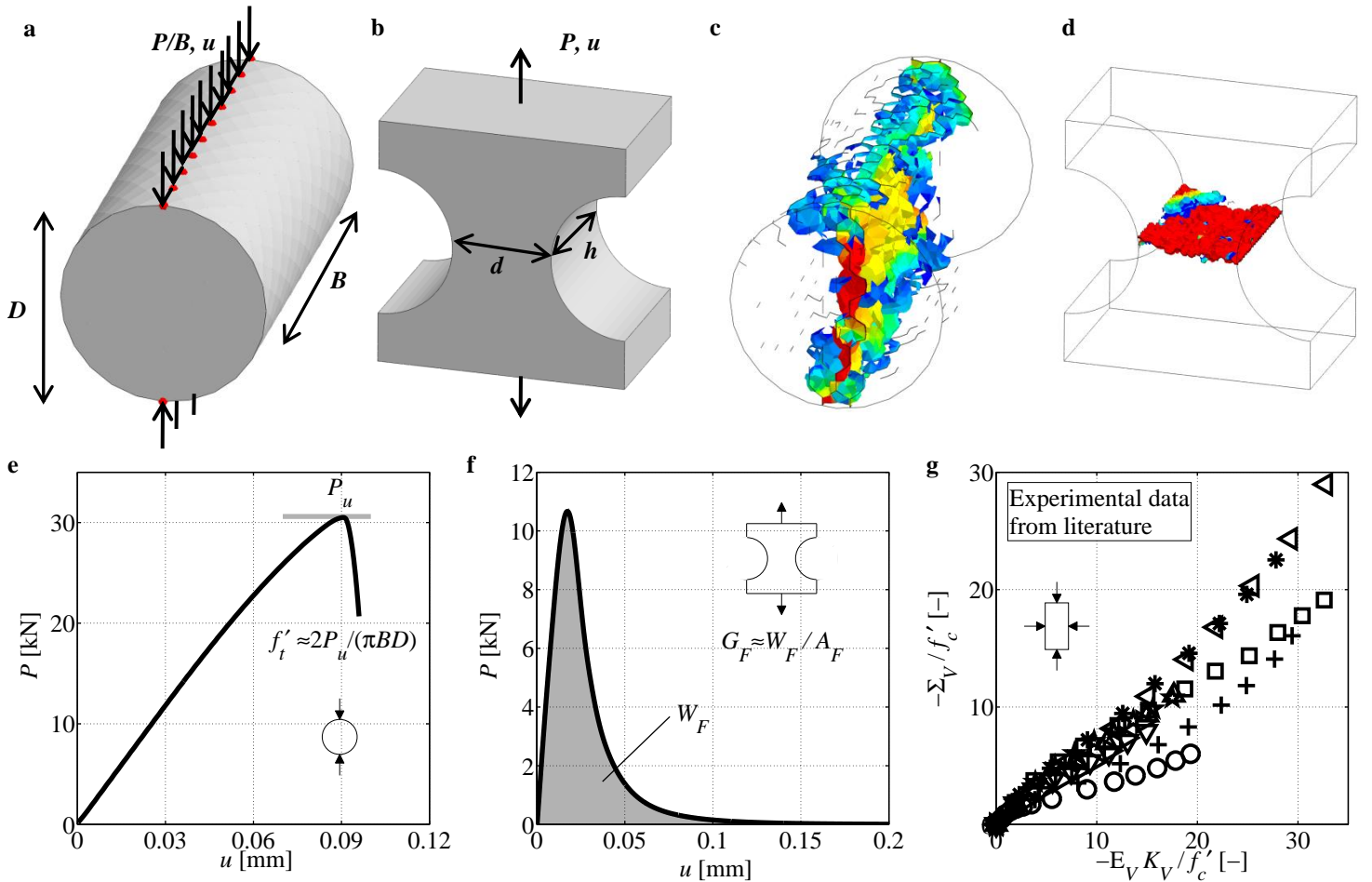


Figure 1: a) Setup for splitting tests; b) Setup for direct tension test on dogbone specimens; c) Contours of meso-scale crack opening at failure for splitting tests; d) Contours of meso-scale crack opening at failure for direct tension tests; e) Typical load-displacement curve for splitting tests; f) Typical load-displacement curve for direct tension tests; g) Typical experimental data for hydrostatic compression tests.

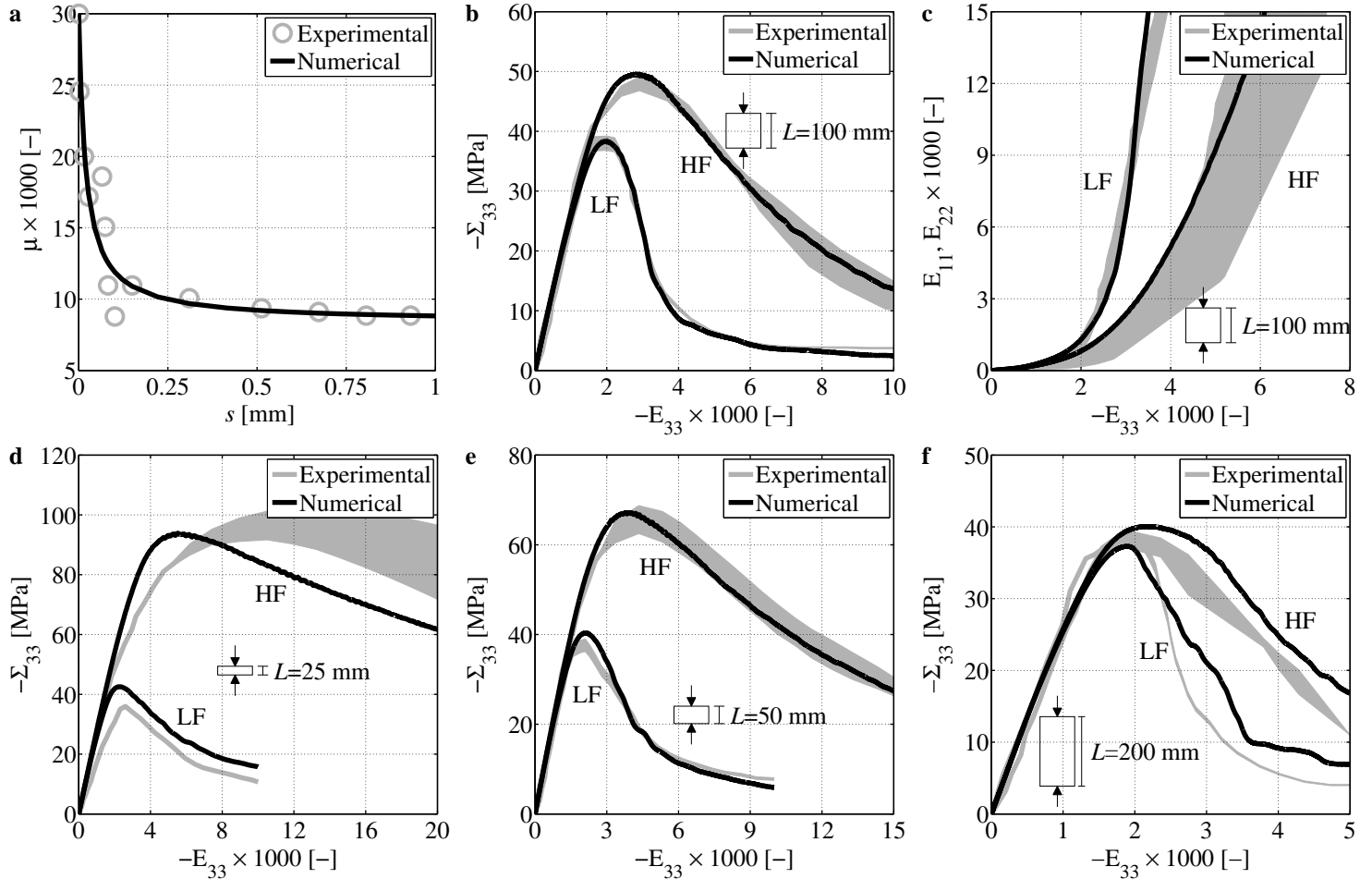


Figure 2: Unconfined compression behavior. a) Low friction coefficient; b) Macroscopic stress-strain curves for cubes; c) Lateral expansion for cubes; d) Macroscopic stress-strain curves for very short prisms; e) Macroscopic stress-strain curves for short prisms; f) Macroscopic stress-strain curves for long prisms.

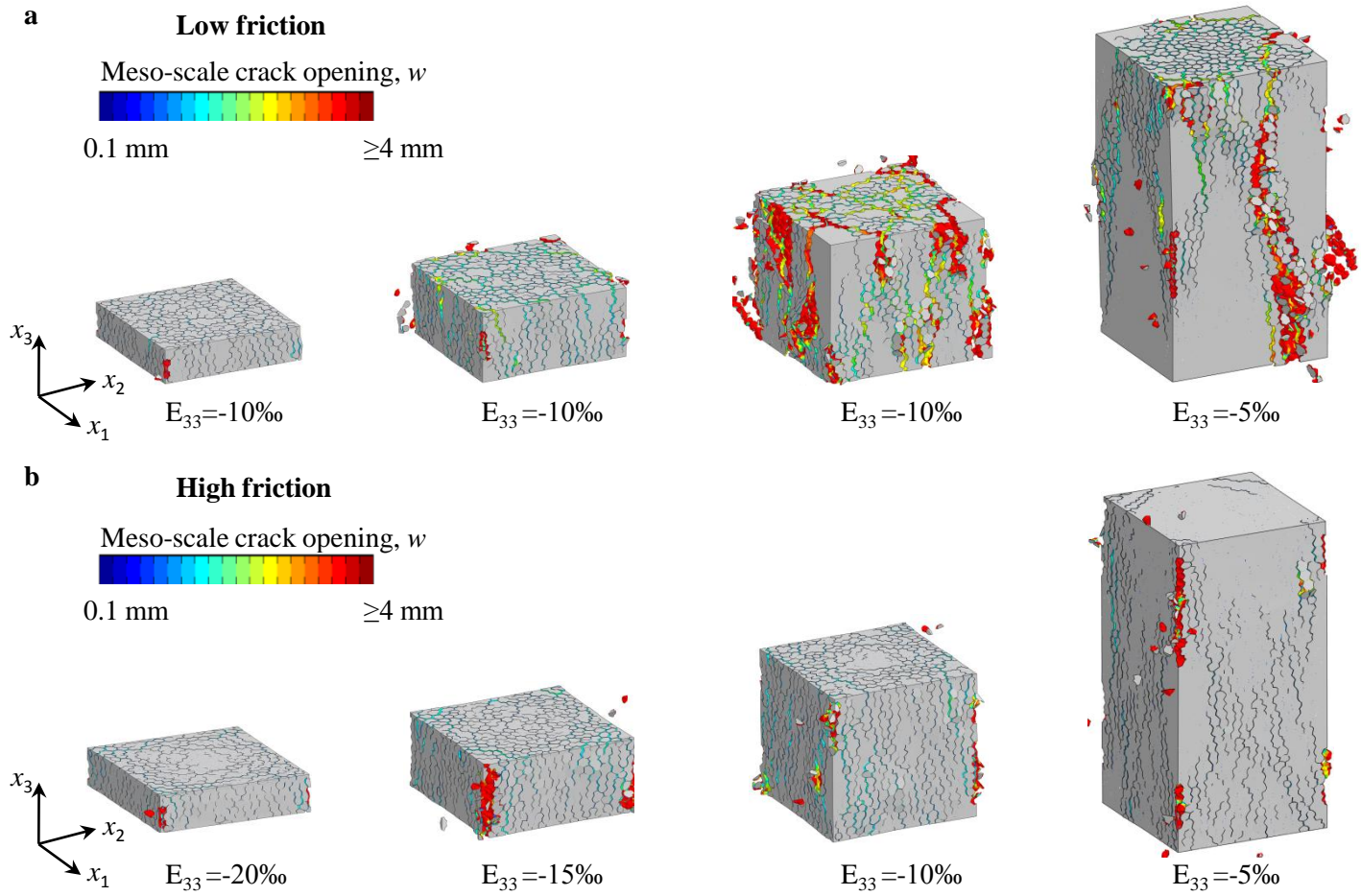


Figure 3: Unconfined compression behavior. a) Contours of meso-scale crack opening at failure for low friction boundary conditions; b) Contours of meso-scale crack opening at failure for high friction boundary conditions.

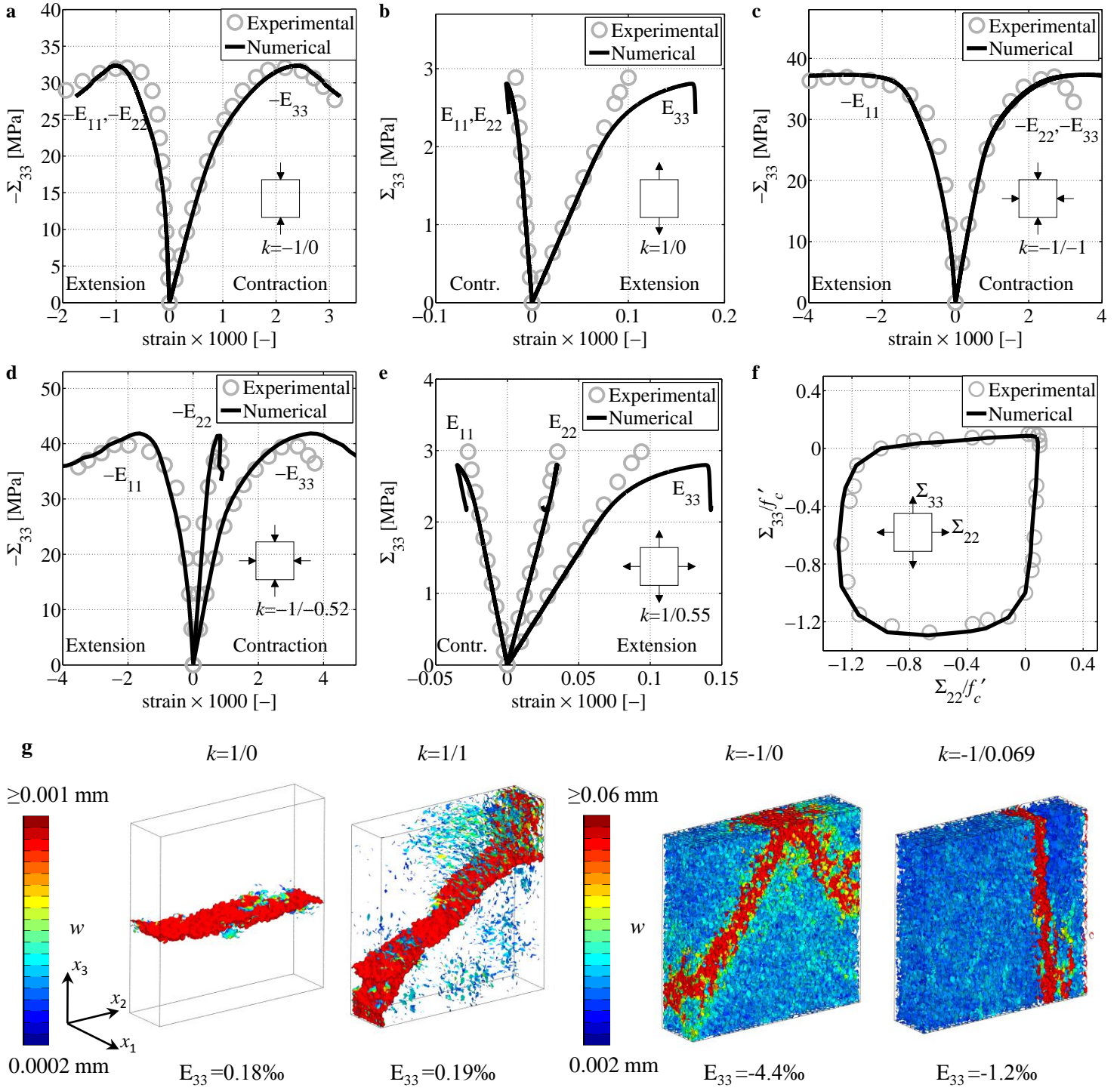


Figure 4: Biaxial Behavior. Macroscopic stress-strain curves for a) uniaxial compression; b) uniaxial tension; c) equibiaxial compression; d) biaxial compression; e) biaxial tension. f) Biaxial failure envelope. g) Contours of meso-scale crack opening at failure for different biaxial loading paths.

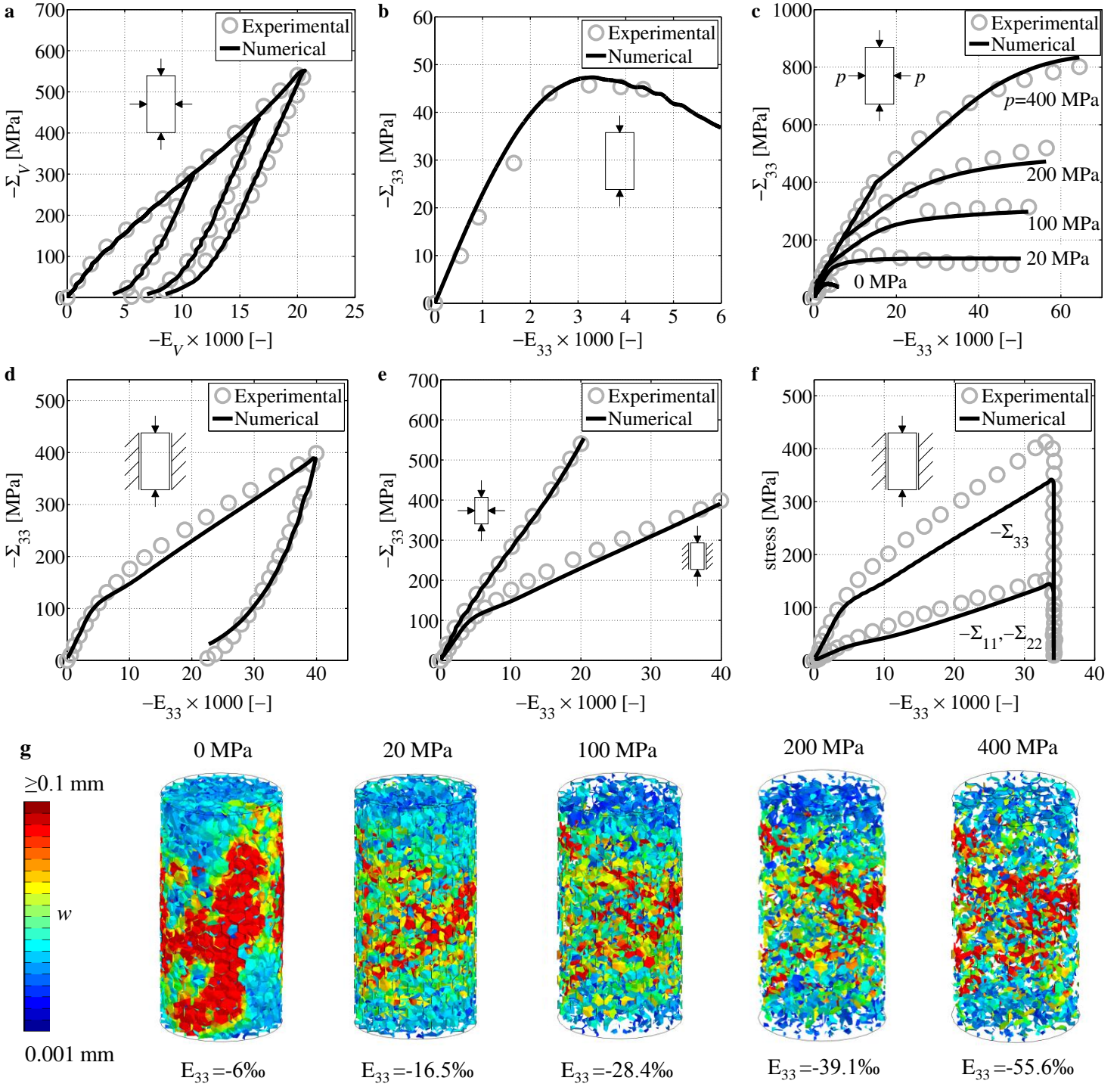


Figure 5: Triaxial compression behavior at high-confinement. Macroscopic stress-strain curves for a) hydrostatic compression; b) uniaxial unconfined compression; c) triaxial compression; d) confined (uniaxial strain) compression; e) comparison between hydrostatic and uniaxial strain response; f) confined (uniaxial strain) compression with lateral expansion. g) Contours of meso-scale crack opening at failure.

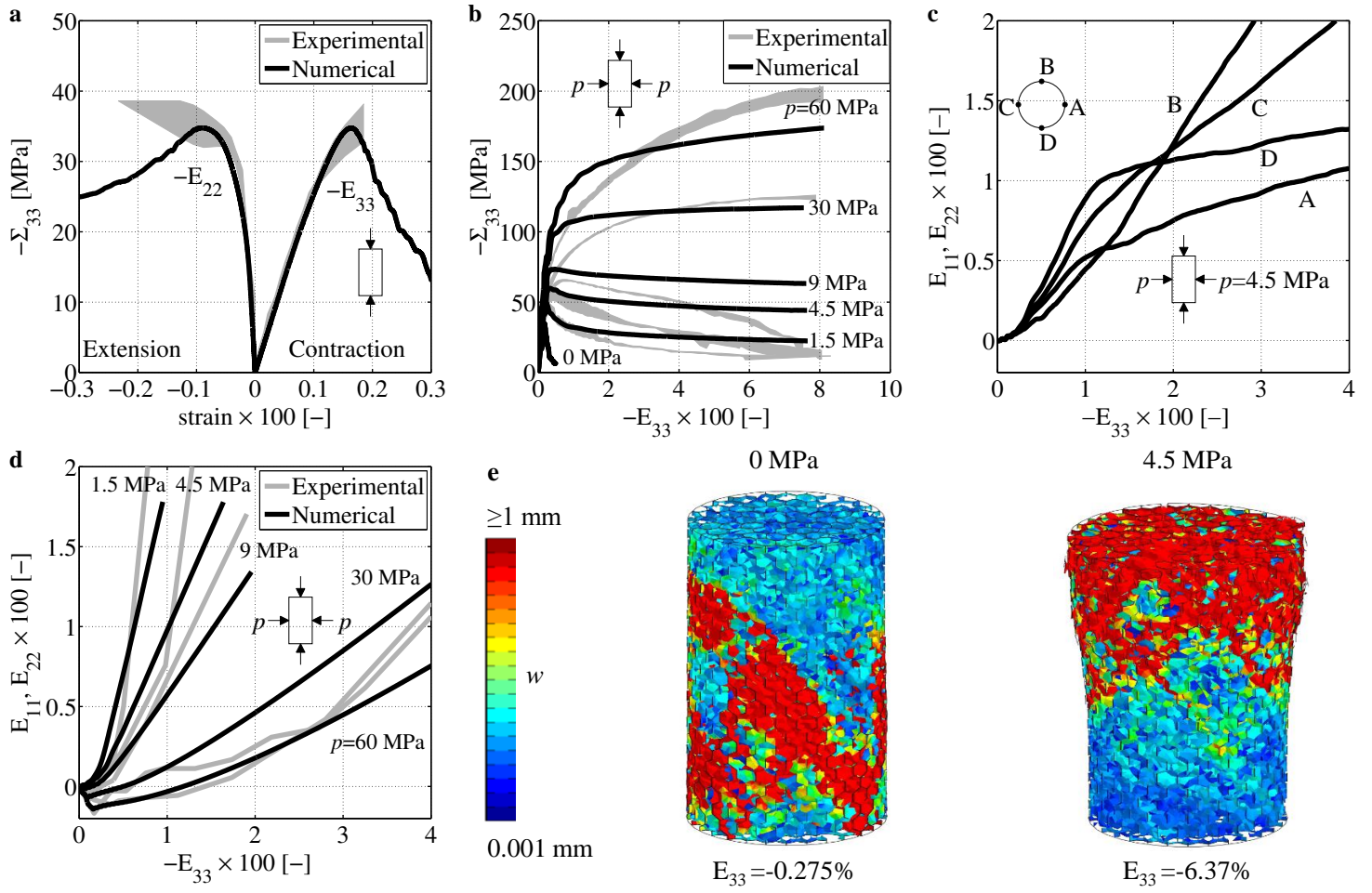


Figure 6: Triaxial compression behavior at low-confinement. Macroscopic stress-strain curves for a) uniaxial unconfined compression; c) triaxial compression. d) Anisotropic lateral expansion under triaxial stress state. e) Contours of meso-scale crack opening at failure.

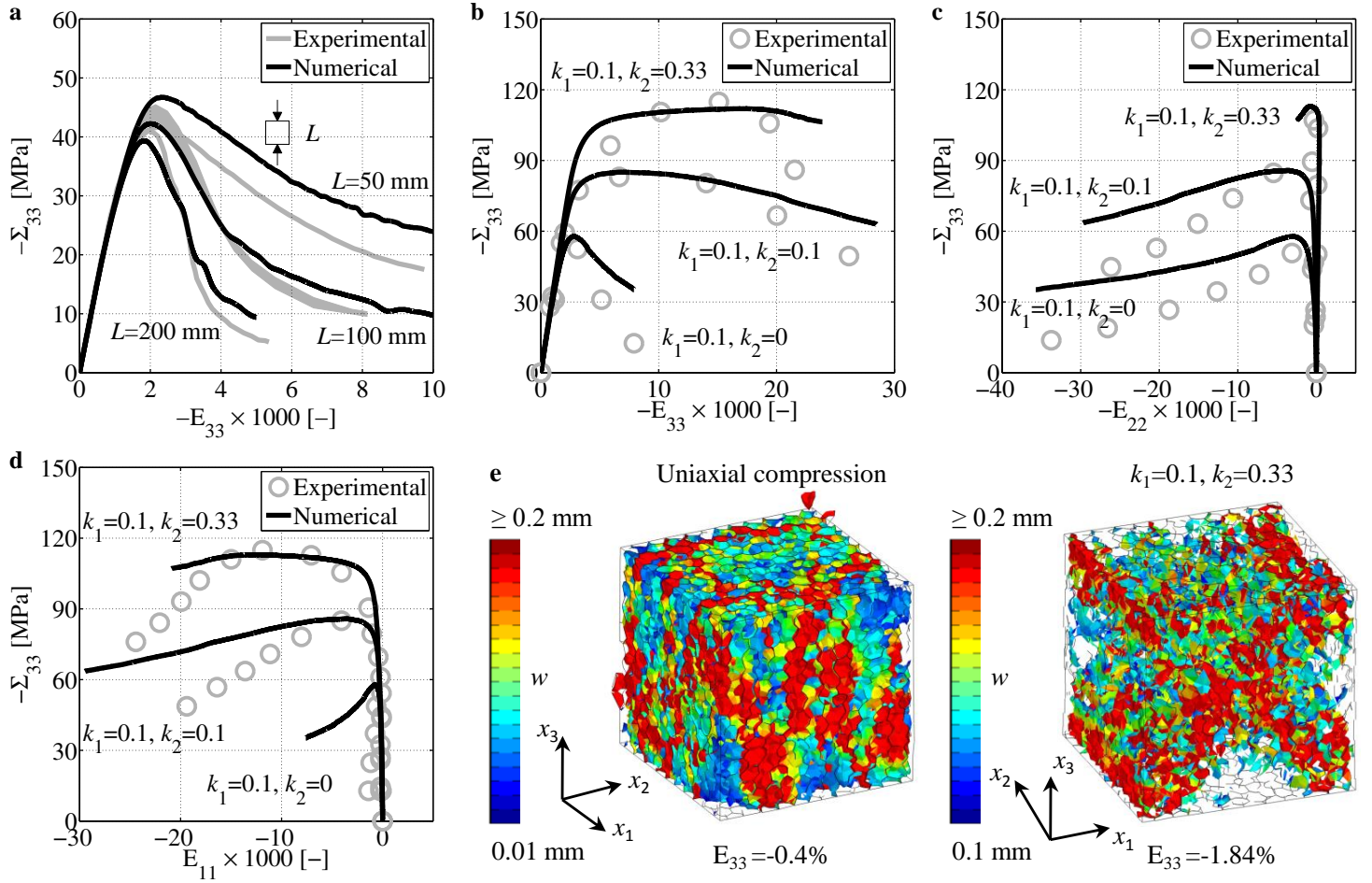


Figure 7: Triaxial behavior under proportional stresses. Macroscopic stress-strain curves for a) unconfined compression; b), c), and d) triaxial compression. e) Contours of meso-scale crack opening at failure.

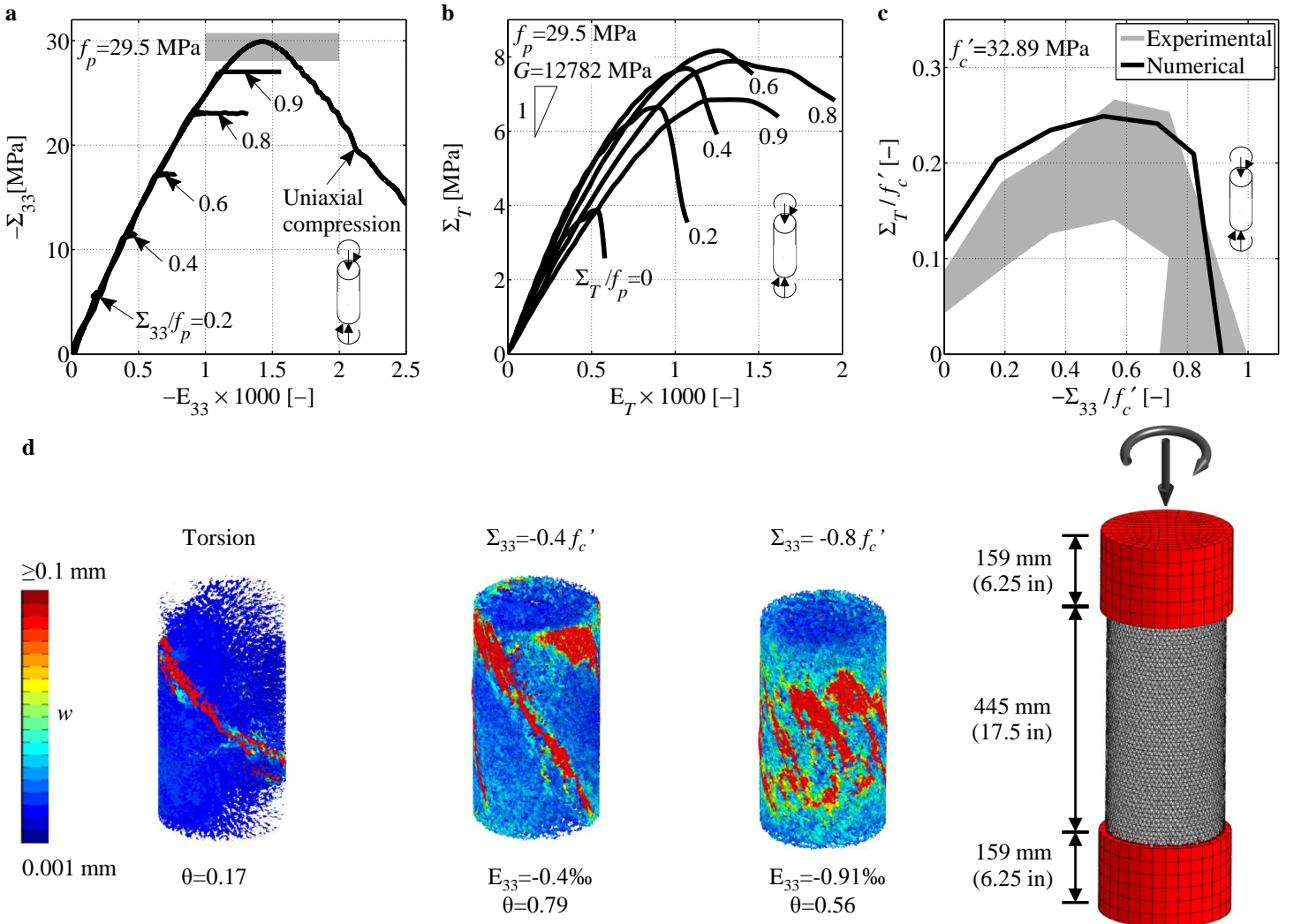


Figure 8: Compression/torsion behavior. Response in terms of macroscopic a) normal stress versus strain curves; b) torsional stress versus strain curves. c) Torsional stress versus compression failure envelope. d) Contours of meso-scale crack opening at failure and test setup.

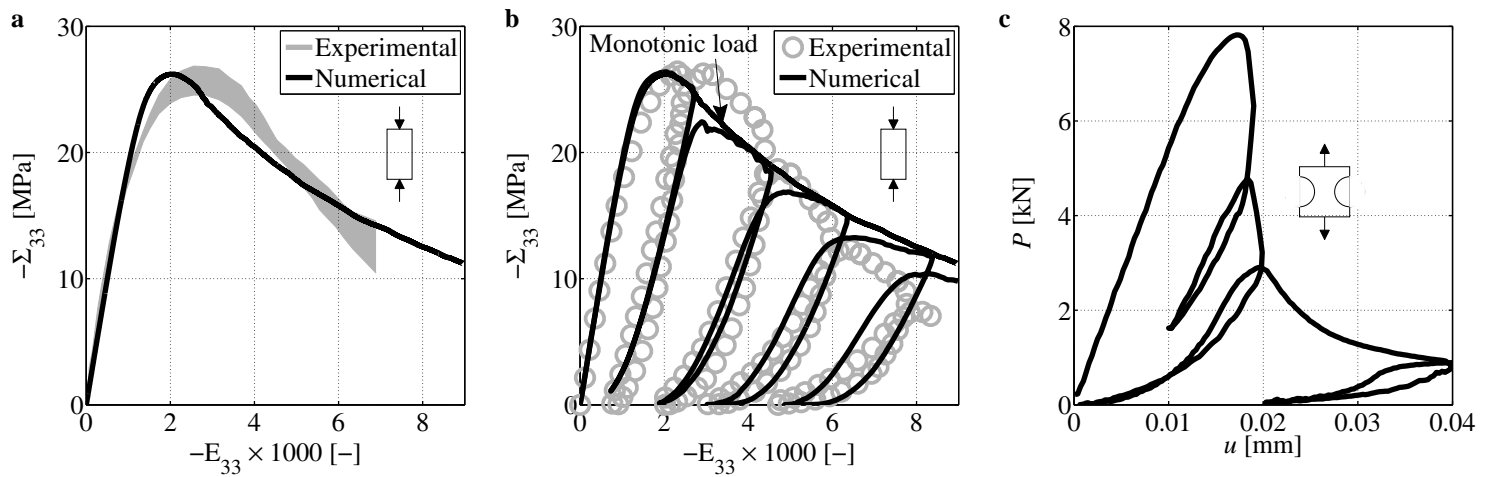


Figure 9: Cyclic compression behavior. Macroscopic stress-strain curves for a) monotonic loading and b) cycling loading. c) Direct tension response for cycling loading.

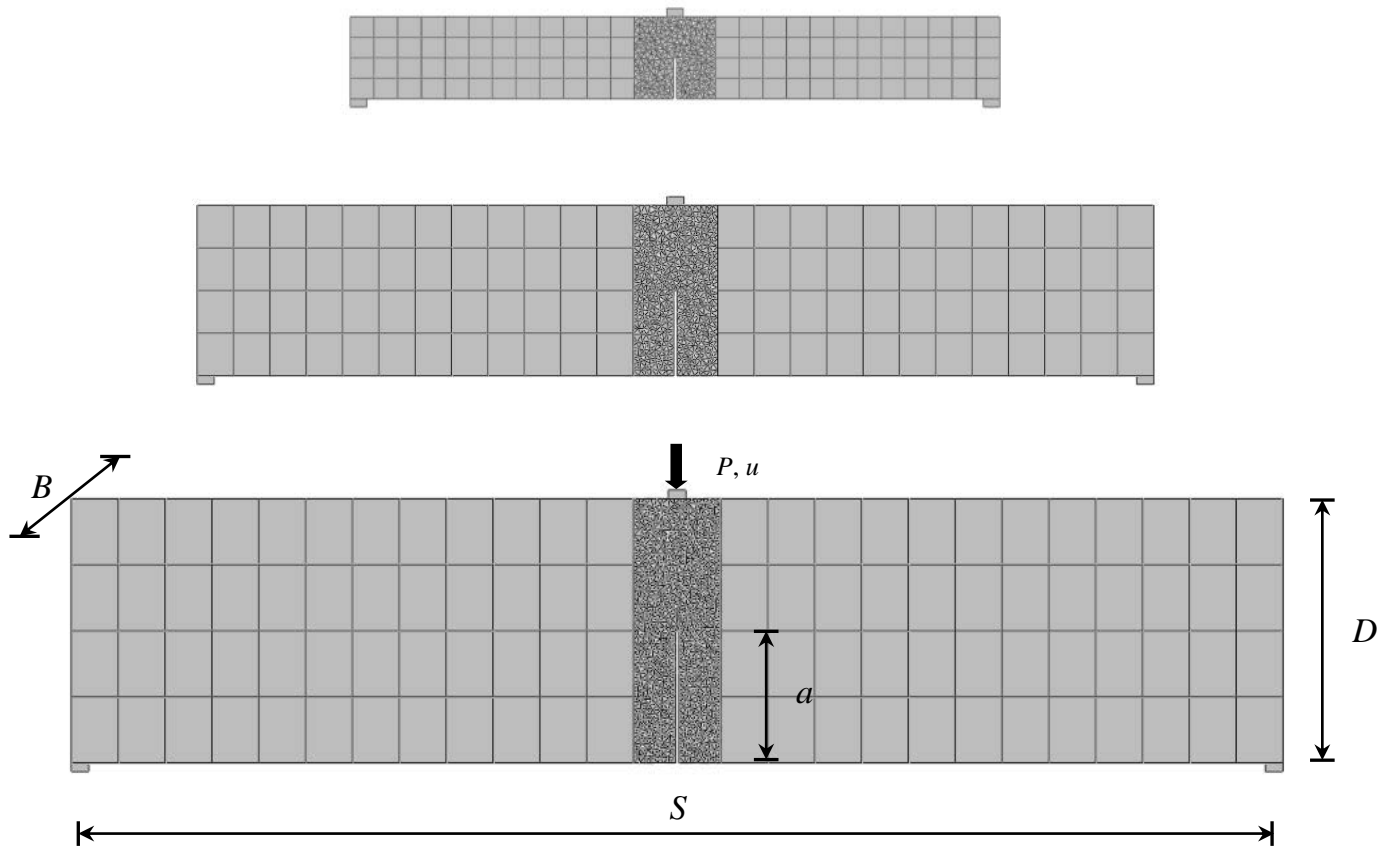


Figure 10: Geometry of three point bending test specimens.

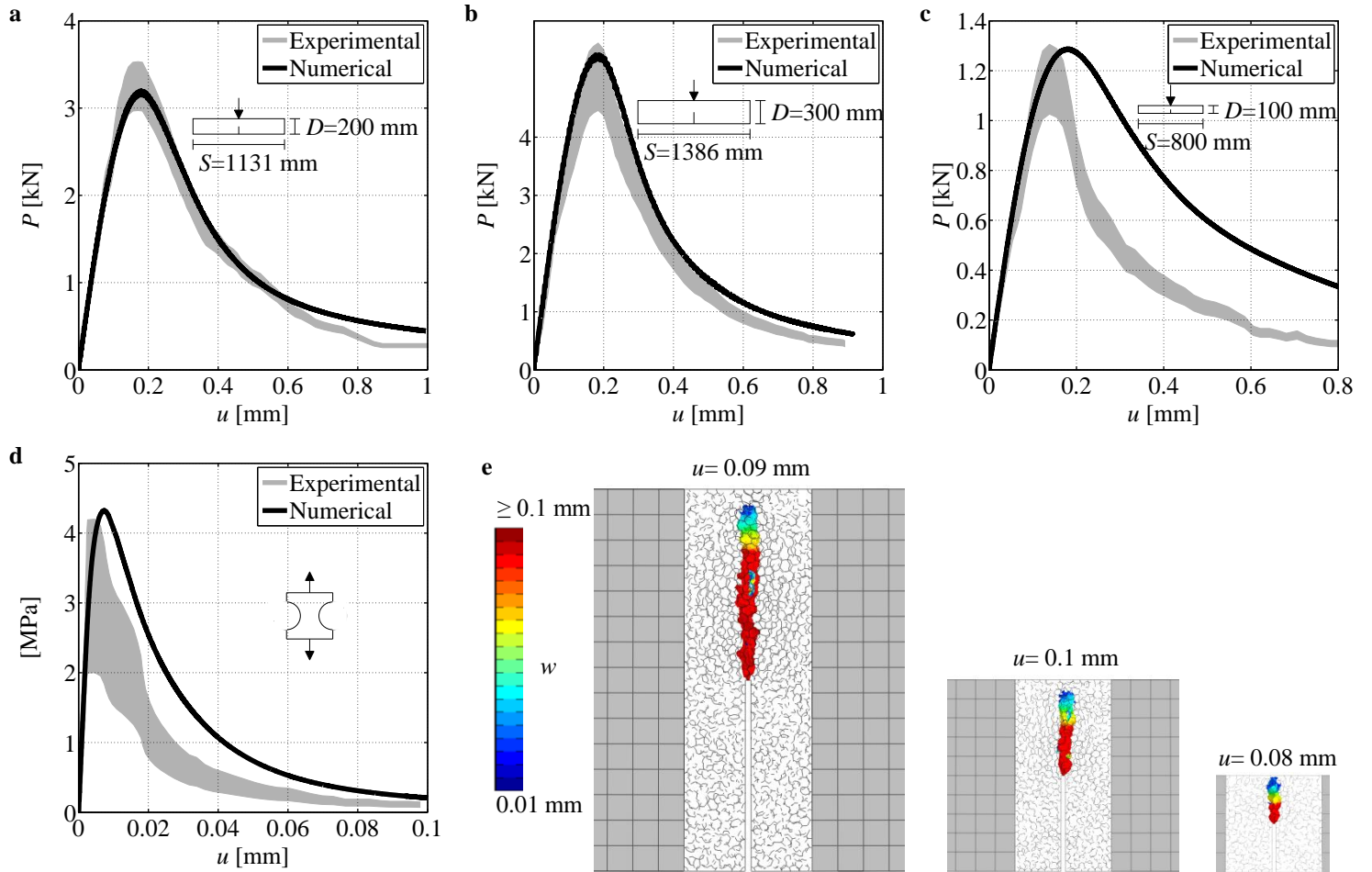


Figure 11: Fracturing behavior. Load-displacement curves for three-point bending tests on a) medium size specimens; b) large size specimens; c) small size specimens. d) Load-displacement curves for direct tension tests on dogbone specimens. e) Contours of meso-scale crack opening at failure.

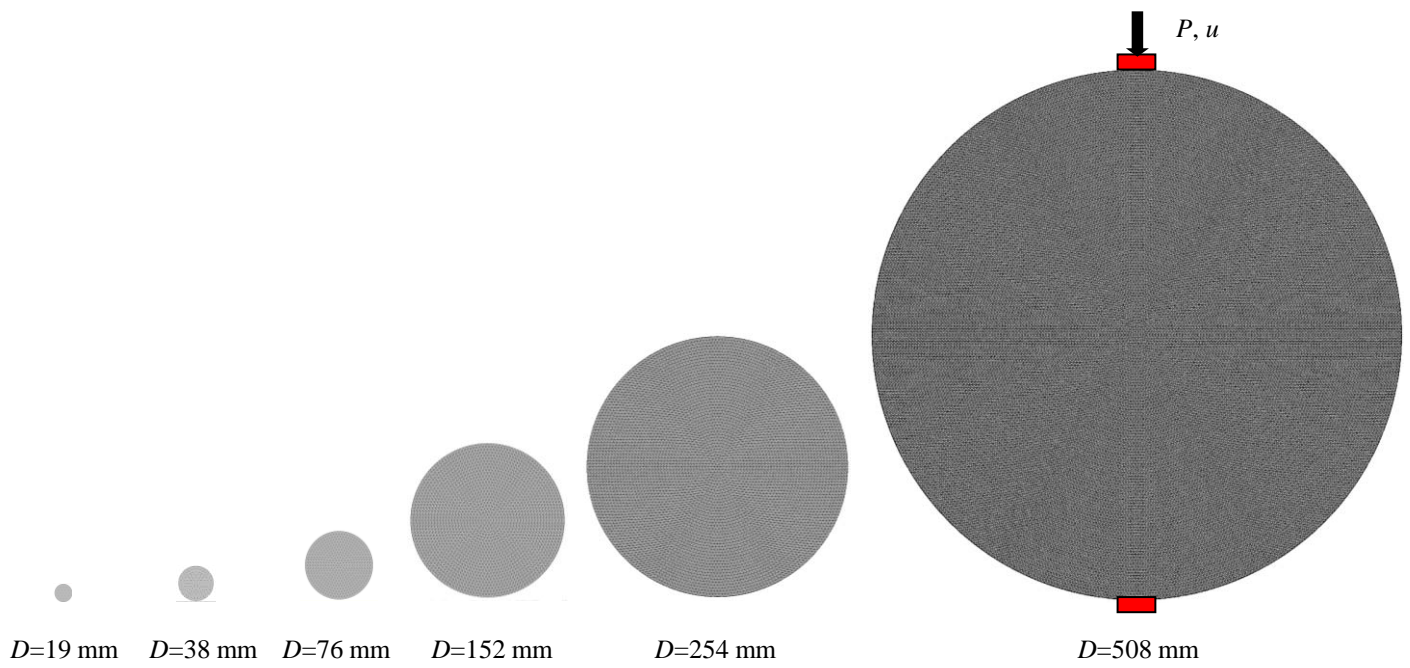


Figure 12: Geometry of the splitting (Brazilian) size effect tests specimens.

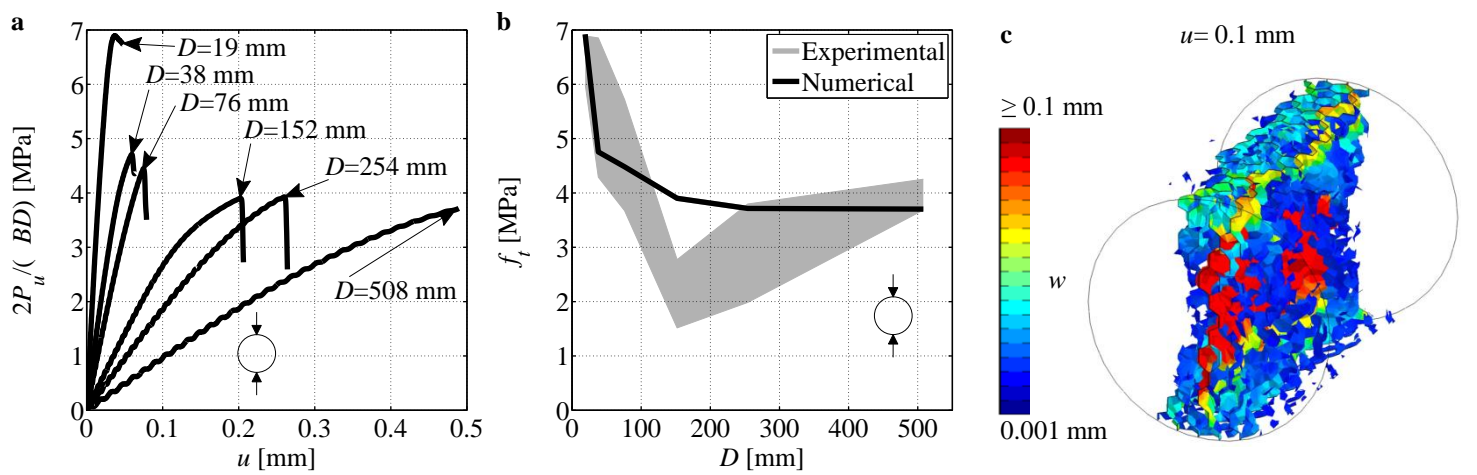


Figure 13: Splitting size-effect tests. a) Nominal macroscopic stress versus displacement. b) Size effect on splitting tensile strength. c) Contours of meso-scale crack opening at failure.